Computers & Structures Vol. 31, No. 4, pp. 607–636, 1989
Printed in Great Britain.

0045-7949/89 $3.00 + 0.00

NUMERICAL ANALYSIS OF CATASTROPHIC SOFTENING BEHAVIOUR (SNAP-BACK INSTABILITY)

ALBERTO CARPINTERI† and GIOVANNI COLOMBO‡
†Department of Structural Engineering, Politecnico di Torino, 10129 Torino, Italy
‡ENEL-CRIS, 20162 Milano, Italy

(*Received* 20 *January* 1988)

Abstract—The nature of crack and structure behaviour can range from ductile to brittle in dependence on material properties, structure geometry, loading conditions and external constraints. The influence of variation in fracture toughness, tensile strength and geometric size scale are investigated on the basis of the π-Theorem of dimensional analysis. Strength and toughness present in fact different physical dimensions and any consistent fracture criterion must describe energy dissipation per unit volume and per unit crack area respectively. A cohesive crack model is proposed, which aims to describe the size effects of fracture mechanics, i.e. the transition from ductile to brittle structure behaviour, by increasing the size scale and keeping the geometric shape unchanged.

For extremely brittle cases (e.g. initially uncracked specimens, large and/or slender structures, low fracture toughness, high tensile strength, etc.) a snap-back in the equilibrium path occurs and the load–deflection softening branch assumes a positive slope. Both load and deflection must decrease to obtain slow and controlled crak propagation (whereas in normal softening only the load must decrease). If the loading process is deflection-controlled, the loading capacity presents a discontinuity with a negative jump. It is proved that such a catastrophic event tends to reproduce the classical LEFM-instability ($K_I = K_{IC}$) for small fracture toughnesses and/or for large structure sizes. In these cases, neither plastic zone development nor slow crack growth occurs before unstable crack propagation.

1. INTRODUCTION

Crack growth in real structures is often stable and develops slowly with initially partial and then total stress-relaxation at the crack tip. Only in some particular cases does crack formation and/or propagation occur suddenly with a catastrophic drop in the load-carrying capacity. The nature of crack and structure behaviour can range from ductile to brittle in dependence on material properties, structure geometry, loading condition and external constraints. The influence of variation in fracture toughness, tensile strength and geometric size scale may be investigated on the basis of the π-Theorem of dimensional analysis [1–3]. Strength and toughness parameters present, in fact, different physical dimensions and any consistent fracture criterion and numerical model must describe energy dissipation per unit volume and per unit crack area respectively [4].

When the fracture phenomenon is extremely brittle and only energy dissipation on the crack surfaces occurs, LEFM may be properly applied and describe the catastrophic structure behaviour. On the other hand, when the fracture process is extremely ductile and only energy dissipation in the ligament volume develops, Perfectly Plastic Limit Analysis may be conveniently used. The problem arises for intermediate cases, when the fracture process is initially ductile and then brittle and crack propagation is initially slow and then fast and uncontrollable. In those cases, a suitable fracture model must be adopted. In the present paper a cohesive crack model is proposed, with the aim of describing the size effects of fracture mechanics, i.e. the transition from ductile to brittle structure behaviour, only by increasing the size scale and keeping the geometric shape unchanged.

For extremely brittle cases (e.g., initially uncracked specimens, large and/or slender structures, low fracture toughness, high tensile strength, etc.) a bifurcation in the equilibrium path occurs and the load P–deflection δ softening branch assumes a positive slope ($\mathrm{d}P/\mathrm{d}\delta > 0$). This means that both load and deflection must decrease to obtain slow and controlled crack propagation, whereas in normal softening ($\mathrm{d}P/\mathrm{d}\delta < 0$) only the load must decrease. If, in the former situation, the loading process is deflection-controlled, the P–δ curve presents a discontinuity and the representative point drops on the lower branch with negative slope. It is proved that such a catastrophe tends to reproduce the classical Griffith instability for small fracture toughnesses and/or for large structure sizes.

The accuracy of the numerical description of cohesive crack propagation is also investigated. It is shown that, when the finite element mesh is too coarse, i.e. when the cohesive forces are too far from each other, the cohesive model is unable to describe the fracture process regularly. In other words, when the structure is very large or the fracture toughness very small, the plastic or cohesive zone at the crack tip becomes relatively small and the finite element mesh must be refined, so that such a zone and the LEFM-stress-singularity can be reproduced and the equilibrium branching described.

For each critical value of strain energy release rate G_{IC}, an upper bound to the finite element size exists, beyond which the numerical representation is irregular. Vice versa, for each finite element size a lower bound to G_{IC} exists, below which the P–δ curve is not reproducible. Such considerations are extended to the non-dimensional field and it is shown that, for low fracture toughnesses and/or large structure sizes, the loading capacity can be provided by the well-known condition $K_I = K_{IC}$. In these cases, it is not convenient to use a cohesive crack model with a huge number of finite elements. It is much more economical to apply a LEFM code with the stress-singularity embedded at the crack tip.

2. COHESIVE CRACK MODEL

The cohesive crack model is based on the following assumptions [5–8].

(1) The cohesive fracture zone (plastic or process zone) begins to develop when the maximum principal stress achieves the ultimate tensile strength σ_u (Fig. 1a).

(2) The material in the process zone is partially damaged but still able to transfer stress. Such a stress is dependent on the crack opening displacement w (Fig. 1b).

The real crack tip is defined as the point where the distance between the crack surfaces is equal to the critical value of crack opening displacement w_c, and the normal stress vanishes (Fig. 2a). On the other hand, the fictitious crack tip is defined as the point where the normal stress attains the maximum value σ_u and the crack opening vanishes (Fig. 2a).

The closing stresses acting on the crack surfaces (Fig. 2a) can be replaced by nodal forces (Fig. 2b). The intensity of these forces depends on the opening of the fictitious crack, w, according to the σ–w constitutive law of the material (Fig. 1b). When the

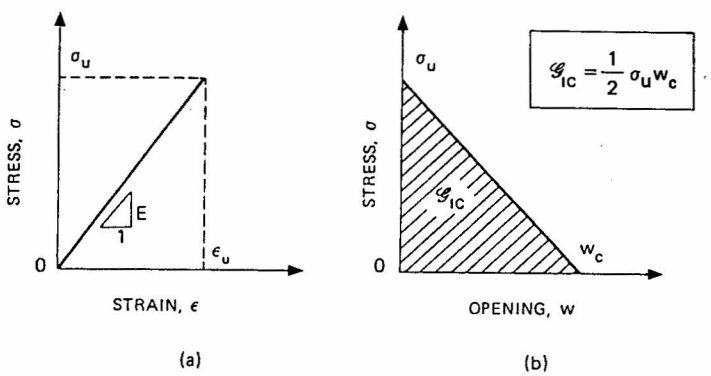

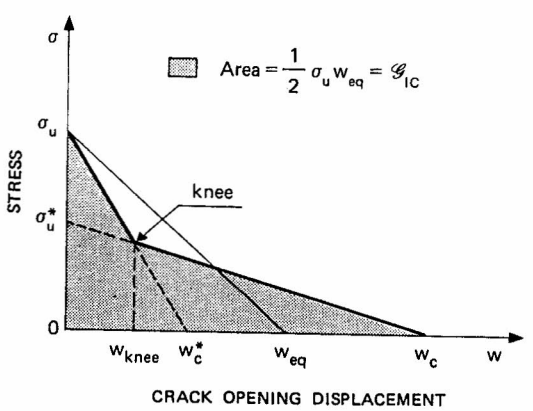

Fig. 1. Stress–strain law (a); linear stress–crack opening displacement law (b); bilinear stress–crack opening displacement law (c).

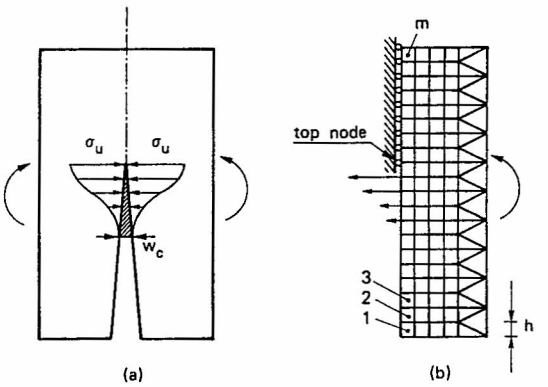

Fig. 2. Stress distribution across the cohesive zone (a) and equivalent nodal forces in the finite element mesh (b).

tensile strength σ_u is achieved at the fictitious crack tip (Fig. 2b), the top node is opened and a cohesive force starts acting across the crack, while the fictitious crack tip moves to the next node.

With reference to the three-point bending test (TPBT) geometry in Fig. 3, the nodes are distributed along the potential fracture line.

The coefficients of influence in terms of node openings and deflection are computed by a finite element analysis, where the fictitious structure in Fig. 3 is subjected to $(n+1)$ different loading conditions. Consider the TPBT in Fig. 4a, with initial crack of length a_0 and tip in node k. The crack opening displacements at the n fracture nodes may be expressed as follows:

$$\mathbf{w} = \mathbf{K}\mathbf{F} + \mathbf{C}P + \boldsymbol{\Gamma}, \tag{1}$$

where

w is the vector of the crack opening displacements,
K is the matrix of the coefficients of influence (nodal forces),
F is the vector of the nodal forces,
C is the vector of the coefficients of influence (external load),
P is the external load,
$\boldsymbol{\Gamma}$ is the vector of the crack opening displacements due to the specimen weight.

On the other hand, the initial crack is stress-free and therefore:

$$F_i = 0, \quad \text{for } i = 1,2,\ldots,(k-1), \tag{2a}$$

while at the ligament there is no displacement discontinuity:

$$w_i = 0, \quad \text{for } i = k, (k+1), \ldots, n. \tag{2b}$$

Equations (1) and (2) constitute a linear algebraic system of $2n$ equations and $2n$ unknowns, i.e. the elements of vectors **w** and **F**. If load P and vector **F** are known, it is possible to compute the beam deflection, δ:

$$\delta = \mathbf{C}^T\mathbf{F} + D_P P + D_\gamma, \tag{3}$$

where D_P is the deflection for $P = 1$ and D_γ is the deflection due to the specimen weight.

After the first step, a cohesive zone forms in front of the real crack tip (Fig. 4b), say between nodes j and l. Then eqns (2) are replaced by

$$F_i = 0, \qquad \text{for } i = 1,2,\ldots,(j-1), \tag{4a}$$

$$F_i = F_u\left(1 - \frac{w_i}{w_c}\right), \qquad \text{for } i = j, (j+1), \ldots, l, \tag{4b}$$

$$w_i = 0, \qquad \text{for } i = l, (l+1), \ldots, n, \tag{4c}$$

where F_u is the ultimate strength nodal force (Fig. 2b):

$$F_u = b\sigma_u/m. \tag{5}$$

Equations (1) and (4) constitute a linear algebraical system of $(2n+1)$ equations and $(2n+1)$ unknowns, i.e. the elements of vectors **w** and **F** and the external load P.

At the first step, the cohesive zone is missing $(l = j = k)$ and the load P_1 producing the ultimate strength nodal force F_u at the initial crack tip (node k) is computed. Such a value P_1, together with the related deflection δ_1 computed through eqn. (3), gives the first point of the P–δ curve. At the second step, the cohesive zone is between the nodes k and $(k+1)$,

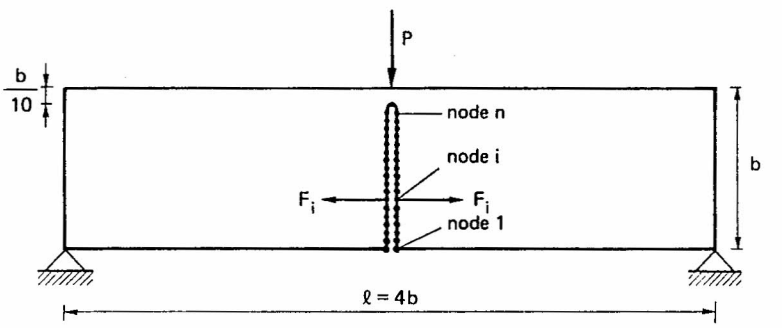

Fig. 3. Finite element nodes along the potential fracture line.

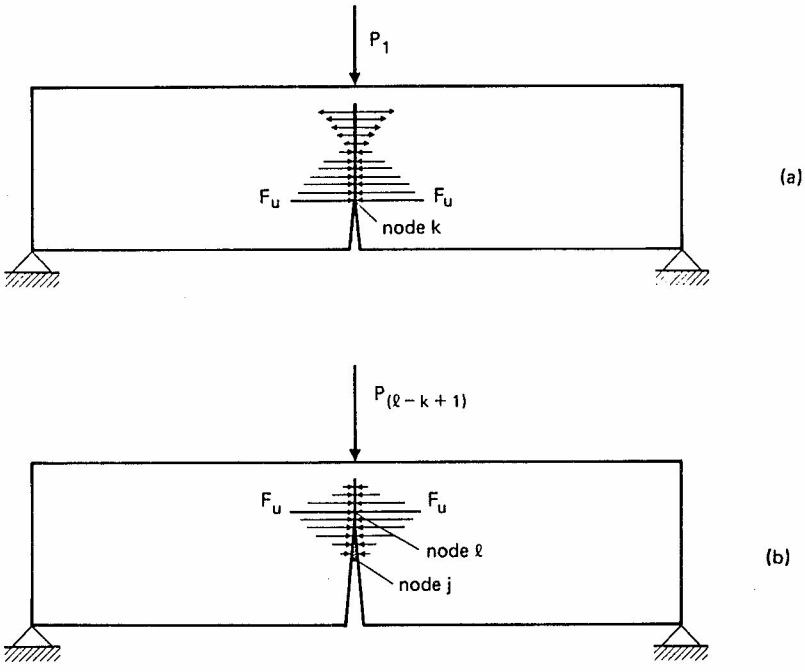

Fig. 4. Cohesive crack configurations at the first (a) and $(1-k+1)$th (b) crack growth increment.

and the load P_2 producing the force F_u at the second fictitious crack tip (node $k+1$) is computed. Equation (3) then provides the deflection δ_2. At the third step, the fictitious crack tip is in the node $(k+2)$, and so on. The present numerical program simulates a loading process where the controlling parameter is the fictitious crack depth. On the other hand, real (or stress-free) crack depth, external load and deflection are obtained at each step after an iterative procedure.

The program stops with the untying of the node n and, consequently, with the determination of the last pair of values F_n and δ_n. In this way, the complete load–deflection curve is automatically plotted by the computer.

3. DUCTILE–BRITTLE TRANSITION AND NUMERICAL ACCURACY IN FINITE ELEMENT ANALYSIS

The accuracy of the numerical description of cohesive crack propagation is investigated in non-dimensional form. For this purpose, the brittleness number s_E is introduced [8–13].

$$s_E = \frac{G_{IC}}{\sigma_u b}, \tag{6}$$

where $G_{IC} = \frac{1}{2}\sigma_u w_c$ is the area under the σ–w curve in Fig. 1(b) and represents the energy necessary to create a unit crack surface, σ_u is the ultimate tensile strength and b is the depth of the beam in Fig. 3. The brittleness number s_E can be put also in the simpler form:

$$s_E = \frac{w_c}{2b}, \tag{7}$$

which is the ratio of the critical crack opening displacement w_c to the characteristic structure size $2b$.

The three-point bending beam in Fig. 3 is considered herein, with the constant geometrical proportions: span $= l = 4b$, thickness $= t = b$. The scale factor is therefore represented by the beam depth b.

As is shown in Fig. 2(b), m finite elements are adjacent to the central line, whereas only $n = 0.9m$ nodes can be untied during crack growth (Fig. 3). The finite element size h (Fig. 2b) is then connected with the beam depth b through the simple relation: $b = mh$.

The three different finite element meshes in Fig. 5 are considered. Mesh (a) presents 20 elements and 18 fracture nodes, mesh (b) 40 elements and 36 fracture nodes, mesh (c) 80 elements and 72 fracture nodes.

The load–deflection response of the three-point bending beam in Fig. 3 is represented in Fig. 6(a–c), for $m = 20$, 40 and 80 respectively. The initial crack depth is assumed $a_0/b = 0.0$, while the ultimate tensile strain $\varepsilon_u = \sigma_u/E$ is 8.7×10^{-5} and the Poisson ratio $\nu = 0.1$. The diagrams are plotted in non-dimensional form by varying the brittleness number s_E. The simple variation in this dimensionless number reproduces all the cases related to the independent variations in G_{IC}, b and σ_u. Not the single values of G_{IC}, b and σ_u, but their function s_E—see eqn. (6)—is responsible for the structural behaviour, which can range from ductile to

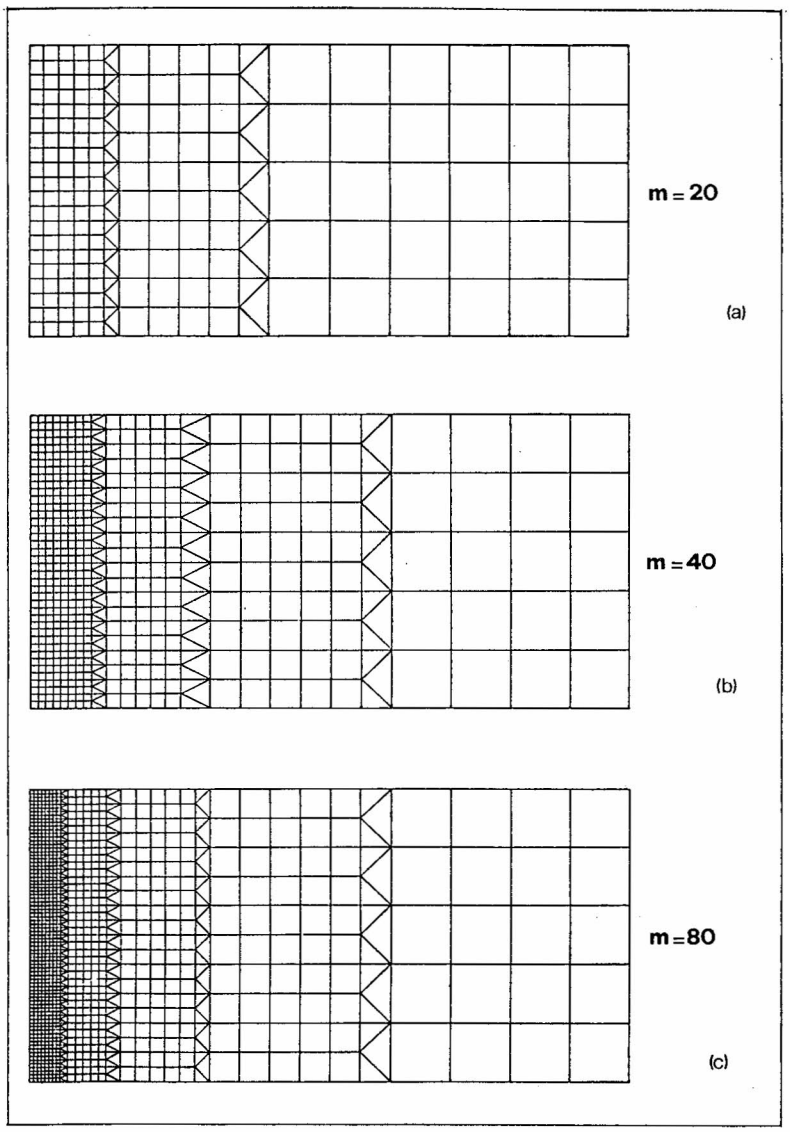

Fig. 5. Refinement of the finite element mesh.

brittle. Specimens with high fracture toughness are then ductile, as well as small specimens and/or specimens with low tensile strength. Vice versa, brittle behaviours are predicted for low fracture toughnesses, large specimens and/or high tensile strengths.

The influence of the variation in the number s_E is investigated over four orders of magnitude in Fig. 6, from 2×10^{-2} to 2×10^{-5}. The results reported in Fig. 6(a–c), appear very similar. Of course, the diagrams for $m = 20$ (Fig. 6a) are slightly less regular than those for $m = 80$ (Fig. 6c), and present some weak cuspidal points, especially for low s_E numbers.

When ulteriorly lower s_E numbers are contemplated, the P–δ diagrams lose their regularity, from a mathematical point of view, and their resolution, from a graphical point of view. The influence of the variation in the s_E number is further analyzed over one order of magnitude in Fig. 7, from 2×10^{-5} to 2×10^{-6}. The results reported in Fig. 7(a–c) appear much less uniform than those in Fig. 6(a–c). The diagrams for $m = 20$ (Fig. 7a) are lacking in mathematical regularity, graphical resolution and physical meaning. The diagrams present a slightly better regularity and resolution for $m = 40$ (Fig. 7b), whereas, for $m = 80$ (Fig. 7c), they appear sufficiently regular, especially when brittleness numbers are not too low ($10^{-5} \lesssim s_E \lesssim 2 \times 10^{-5}$). If a better resolution is requested for $2 \times 10^{-6} \lesssim s_E \lesssim 10^{-5}$, the mesh must be refined, i.e. the number m increased. On the other hand, it is evident that the mesh must be refined, i.e. the cohesive forces must be closer, for relatively large structures and/or relatively brittle materials, where the cohesive zone is confined to a small crack tip region.

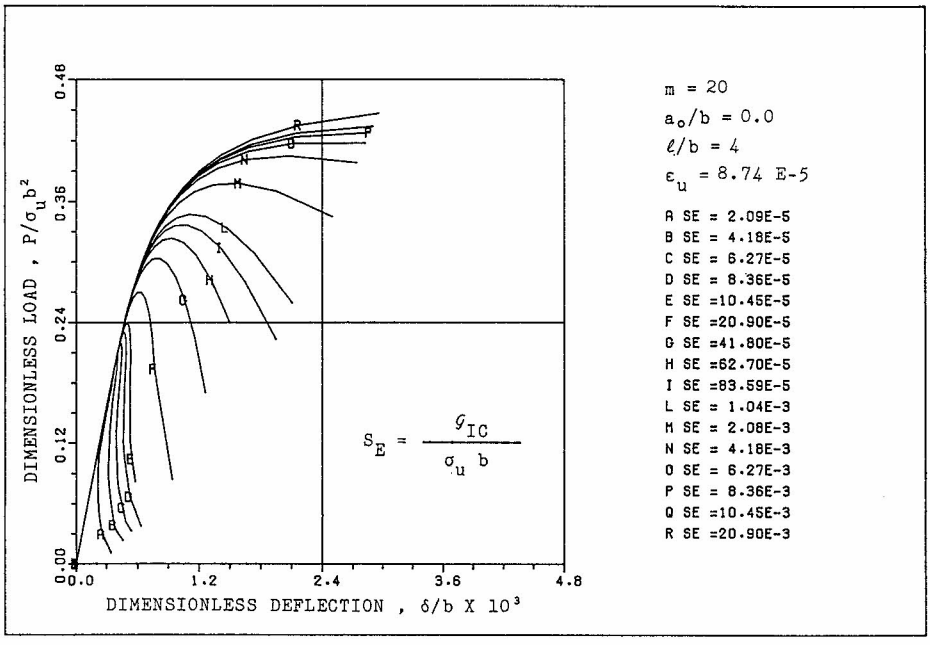
m = 20
a_o/b = 0.0
ℓ/b = 4
ε_u = 8.74 E-5
A SE = 2.09E-5
B SE = 4.18E-5
C SE = 6.27E-5
D SE = 8.36E-5
E SE =10.45E-5
F SE =20.90E-5
G SE =41.80E-5
H SE =62.70E-5
I SE =83.59E-5
L SE = 1.04E-3
M SE = 2.08E-3
N SE = 4.18E-3
O SE = 6.27E-3
P SE = 8.36E-3
Q SE =10.45E-3
R SE =20.90E-3
$S_E = \frac{\mathcal{G}_{IC}}{\sigma_u\, b}$
DIMENSIONLESS LOAD , $P/\sigma_u b^2$
DIMENSIONLESS DEFLECTION , $\delta/b \times 10^3$
0.00
0.12
0.24
0.36
0.48
0.0
1.2
2.4
3.6
4.8

Fig. 6(a).

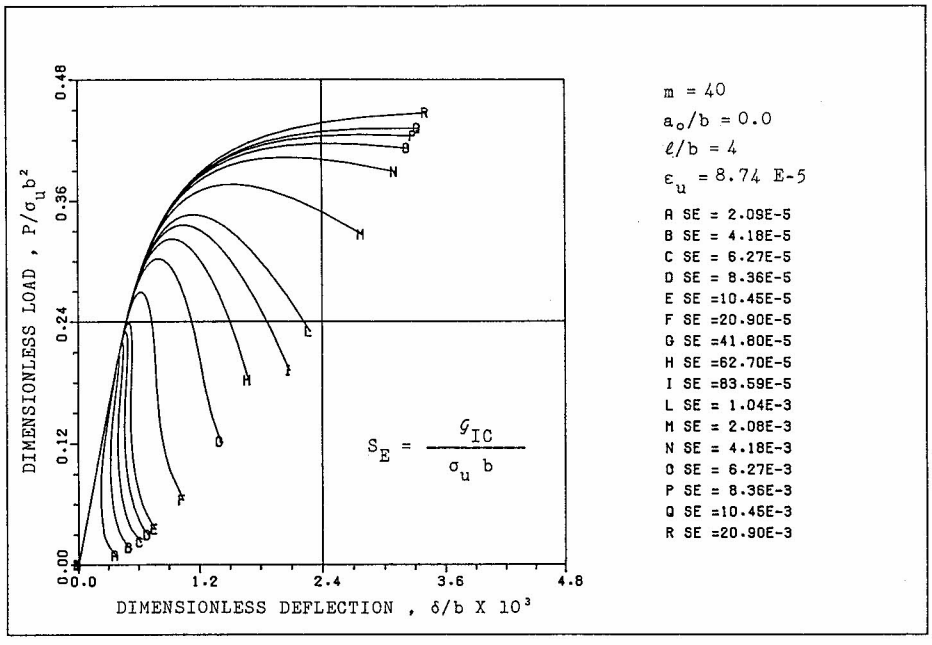
m = 40
a_o/b = 0.0
ℓ/b = 4
ε_u = 8.74 E-5
A SE = 2.09E-5
B SE = 4.18E-5
C SE = 6.27E-5
D SE = 8.36E-5
E SE =10.45E-5
F SE =20.90E-5
G SE =41.80E-5
H SE =62.70E-5
I SE =83.59E-5
L SE = 1.04E-3
M SE = 2.08E-3
N SE = 4.18E-3
O SE = 6.27E-3
P SE = 8.36E-3
Q SE =10.45E-3
R SE =20.90E-3
$S_E = \frac{\mathcal{G}_{IC}}{\sigma_u\, b}$
DIMENSIONLESS LOAD , $P/\sigma_u b^2$
DIMENSIONLESS DEFLECTION , $\delta/b \times 10^3$
0.00
0.12
0.24
0.36
0.48
0.0
1.2
2.4
3.6
4.8

Fig. 6(b).

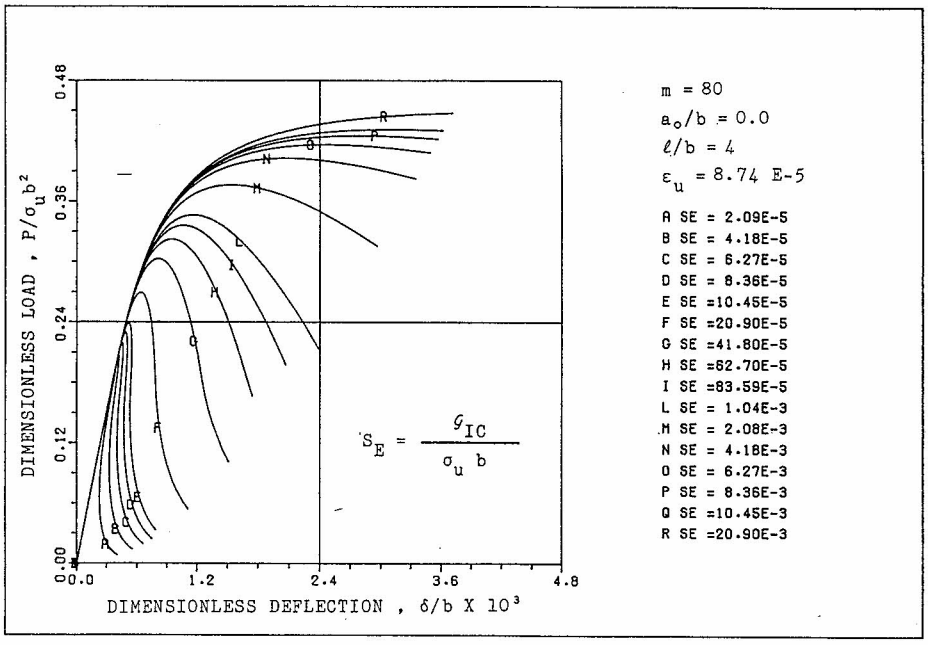

Fig. 6(c).

Fig. 6. Dimensionless load–deflection response of an initially uncracked specimen, by varying the brittleness number, $s_E = G_{IC}/\sigma_u b = w_c/2b$, between 2×10^{-5} and 2×10^{-2}. (a) $m = 20$, (b) $m = 40$, (c) $m = 80$.

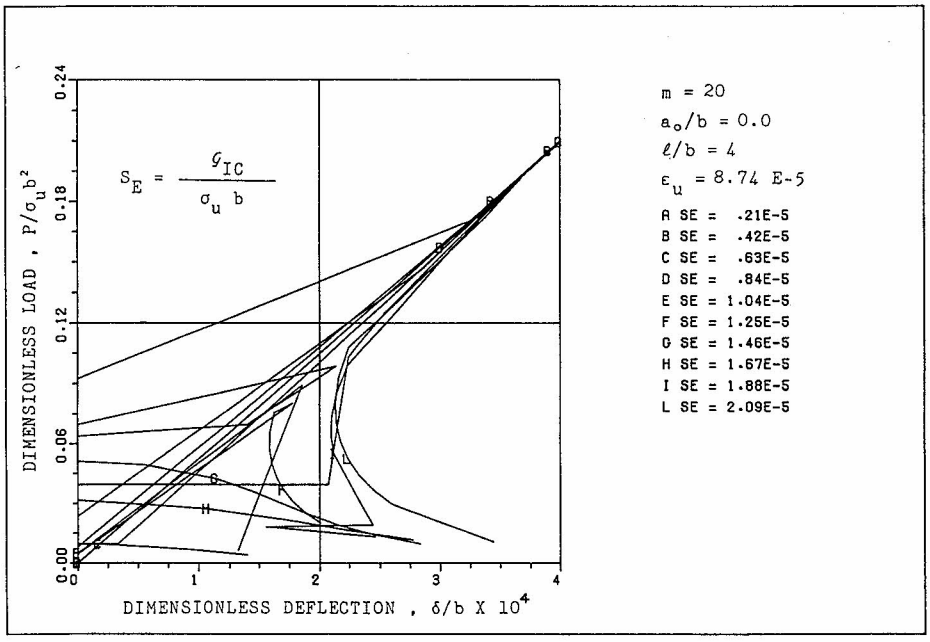

Fig. 7(a).

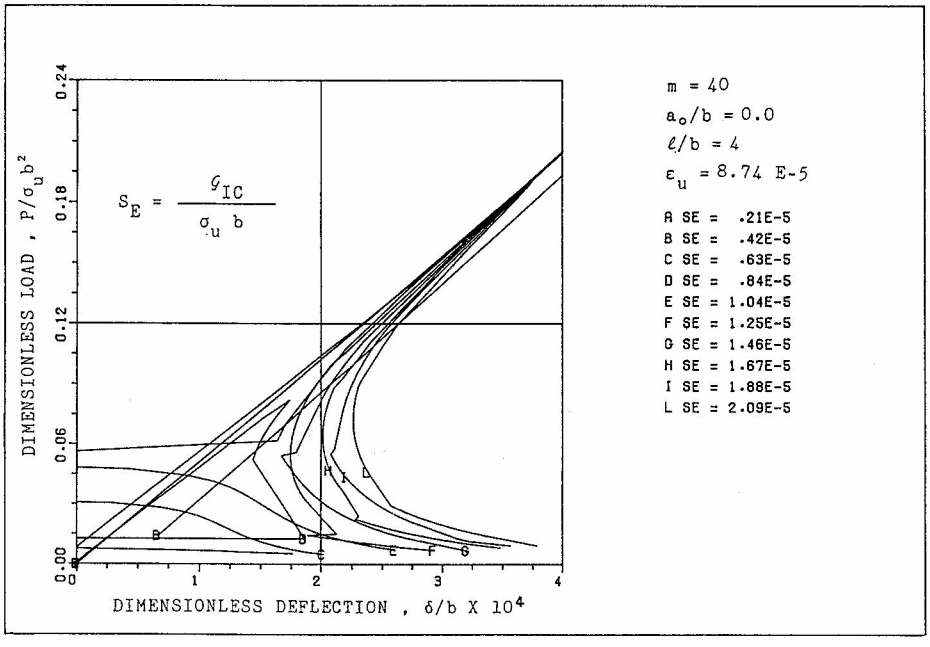

Fig. 7(b).

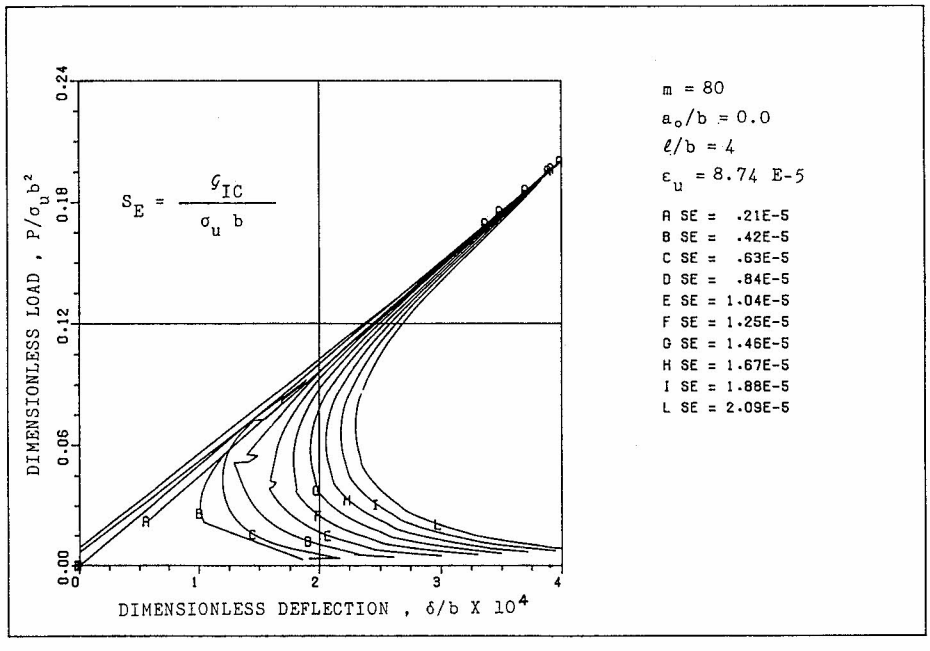

Fig. 7(c).

Fig. 7. Dimensionless load–deflection response of an initially uncracked specimen, by varying the brittleness number, $s_E = G_{IC}/\sigma_u b = w_c/2b$, between 2×10^{-6} and 2×10^{-5}. (a) $m = 20$, (b) $m = 40$, (c) $m = 80$.

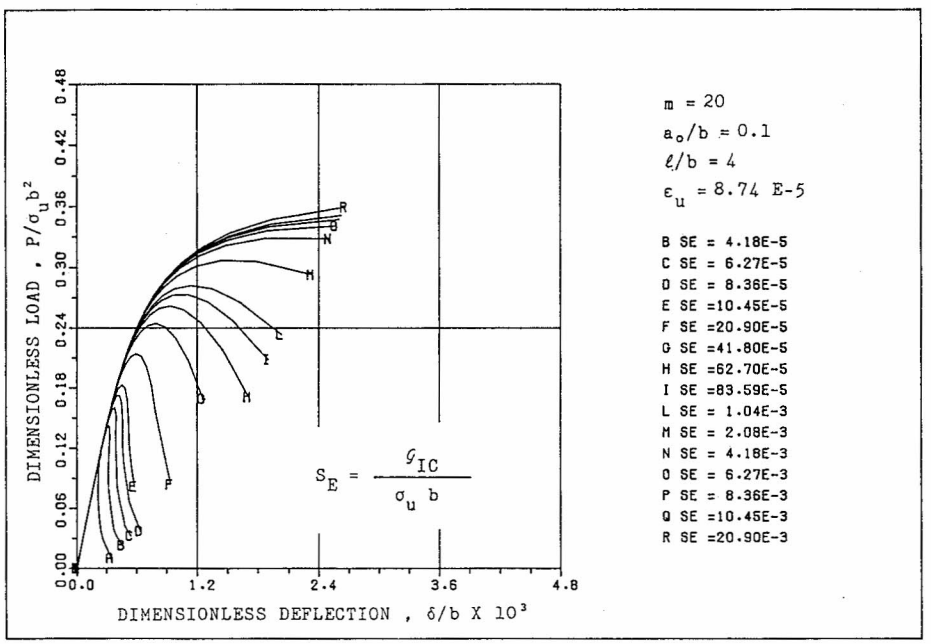
DIMENSIONLESS LOAD , $P/\sigma_u b^2$
0.00
0.06
0.12
0.18
0.24
0.30
0.36
0.42
0.48
0.0
1.2
2.4
3.6
4.8
DIMENSIONLESS DEFLECTION , $\delta/b \times 10^3$
$S_E = \frac{\mathcal{G}_{IC}}{\sigma_u b}$
m = 20
a_o/b = 0.1
ℓ/b = 4
ε_u = 8.74 E-5
B SE = 4.18E-5
C SE = 6.27E-5
D SE = 8.36E-5
E SE =10.45E-5
F SE =20.90E-5
G SE =41.80E-5
H SE =62.70E-5
I SE =83.59E-5
L SE = 1.04E-3
M SE = 2.08E-3
N SE = 4.18E-3
O SE = 6.27E-3
P SE = 8.36E-3
Q SE =10.45E-3
R SE =20.90E-3

Fig. 8(a).

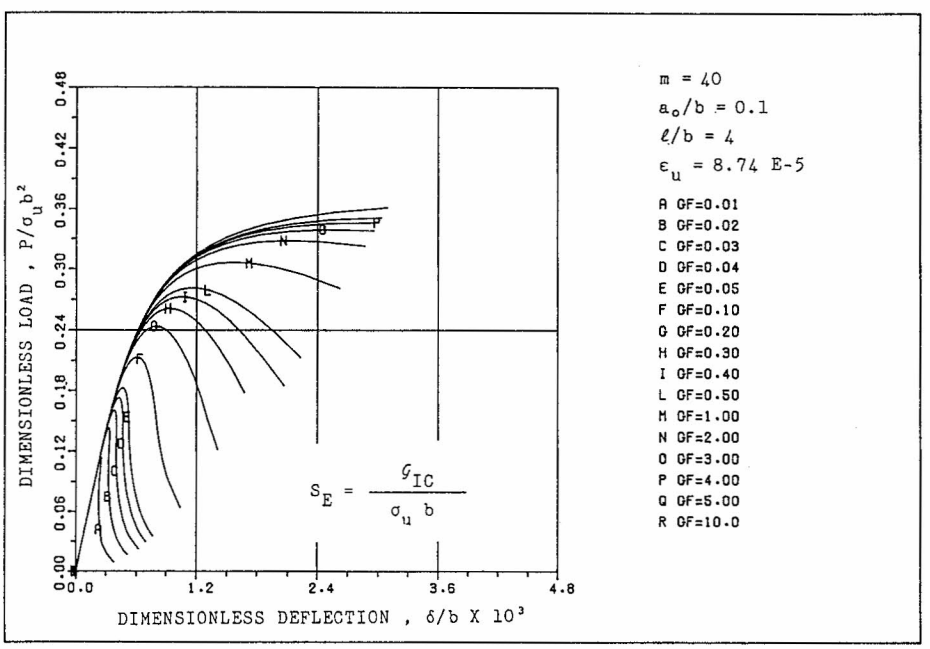
DIMENSIONLESS LOAD , $P/\sigma_u b^2$
0.00
0.06
0.12
0.18
0.24
0.30
0.36
0.42
0.48
0.0
1.2
2.4
3.6
4.8
DIMENSIONLESS DEFLECTION , $\delta/b \times 10^3$
$S_E = \frac{\mathcal{G}_{IC}}{\sigma_u b}$
m = 40
a_o/b = 0.1
ℓ/b = 4
ε_u = 8.74 E-5
A GF=0.01
B GF=0.02
C GF=0.03
D GF=0.04
E GF=0.05
F GF=0.10
G GF=0.20
H GF=0.30
I GF=0.40
L GF=0.50
M GF=1.00
N GF=2.00
O GF=3.00
P GF=4.00
Q GF=5.00
R GF=10.0

Fig. 8(b).

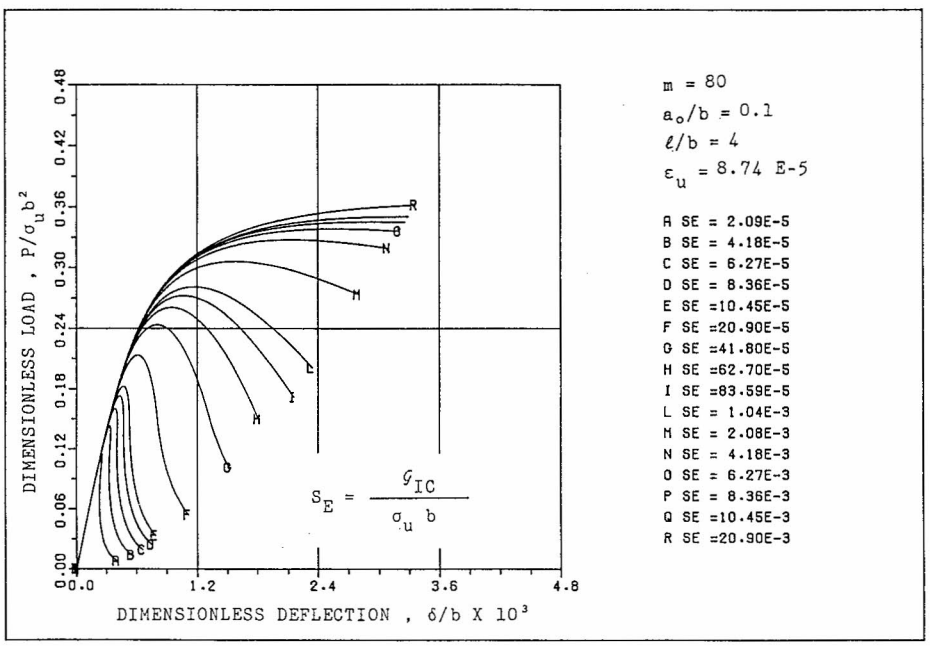

Fig. 8(c).

Fig. 8. Dimensionless load–deflection response of an initially cracked specimen ($a_0/b = 0.1$), by varying the brittleness number, $s_E = G_{IC}/\sigma_u b = w_c/2b$, between 2×10^{-5} and 2×10^{-2}. (a) $m = 20$, (b) $m = 40$, (c) $m = 80$.

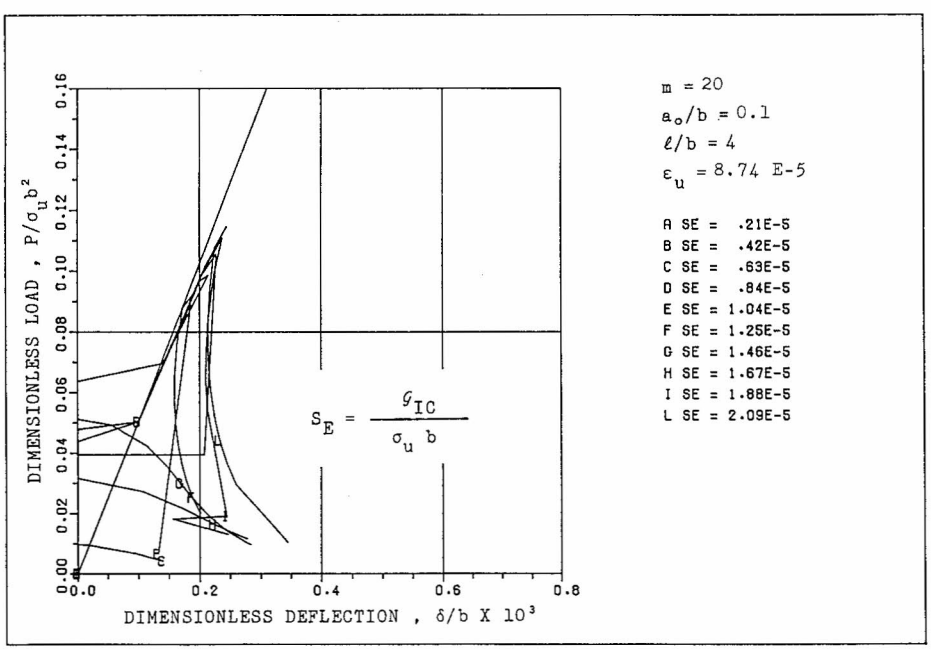

Fig. 9(a).

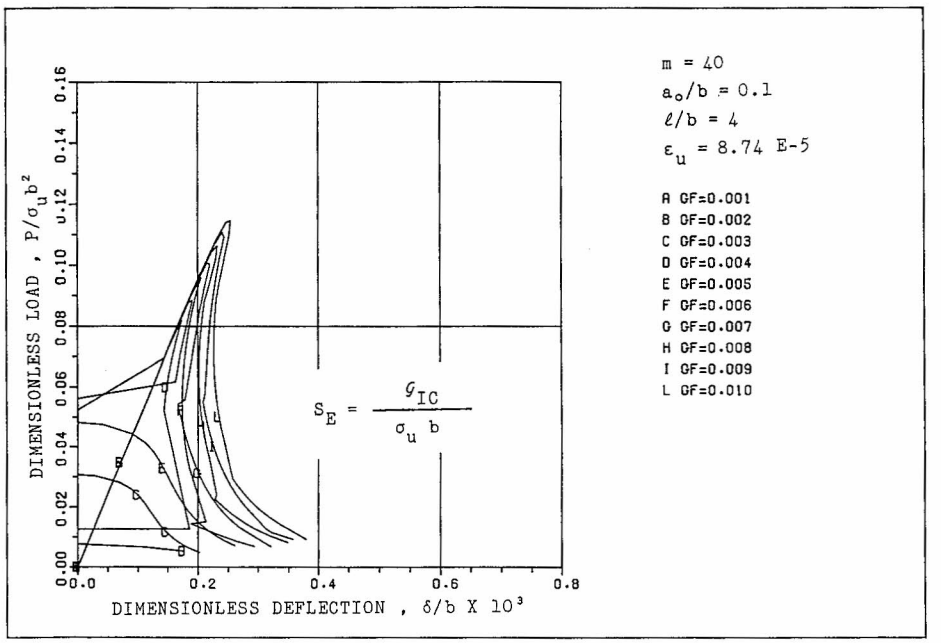

Fig. 9(b).

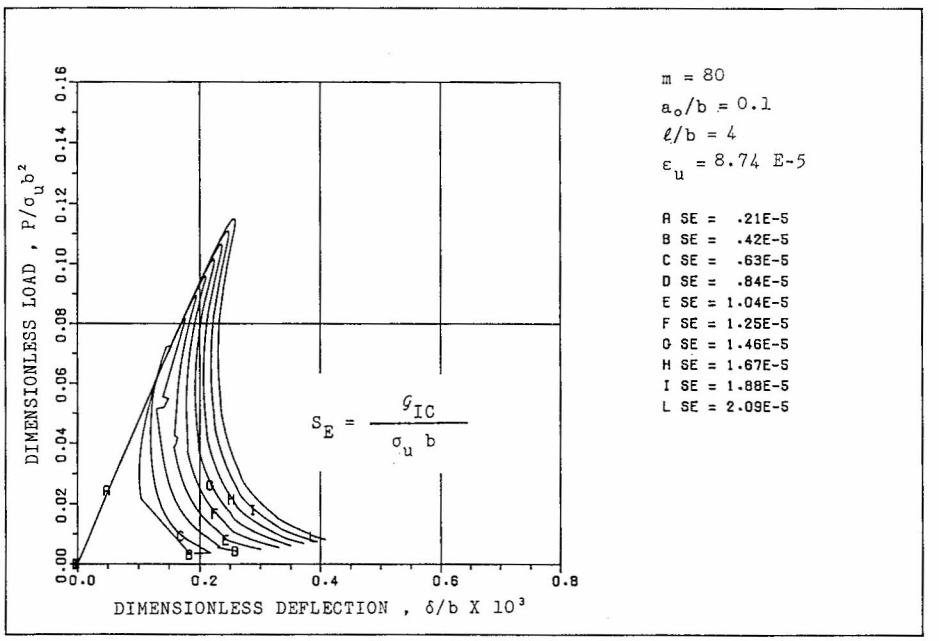

Fig. 9(c).

Fig. 9. Dimensionless load–deflection response of an initially cracked specimen ($a_0/b = 0.1$), by varying the brittleness number, $s_E = G_{IC}/\sigma_u b = w_c/2b$, between 2×10^{-6} and 2×10^{-5}. (a) $m = 20$, (b) $m = 40$, (c) $m = 80$.

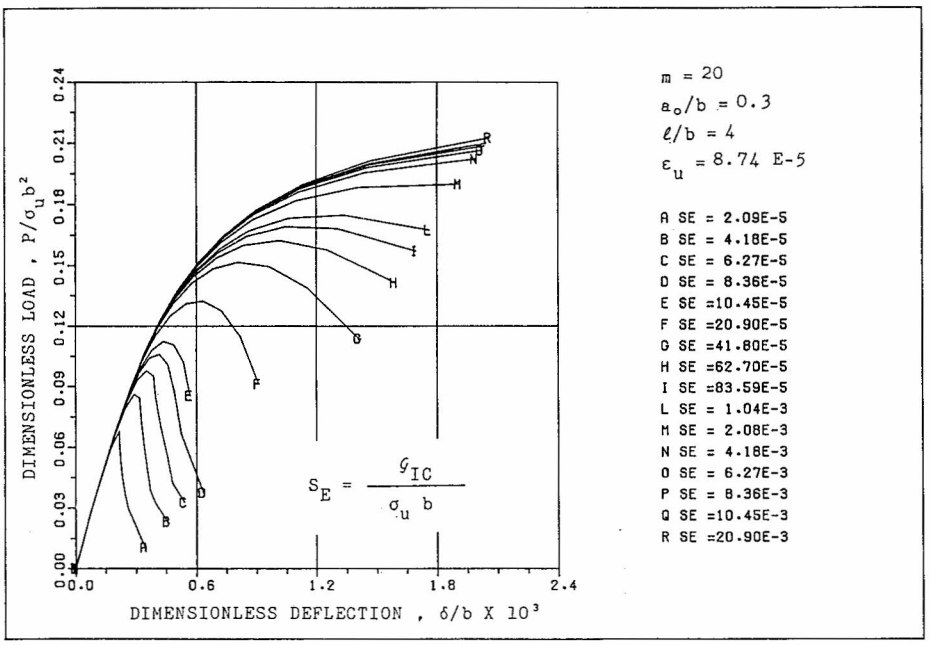

Fig. 10(a).

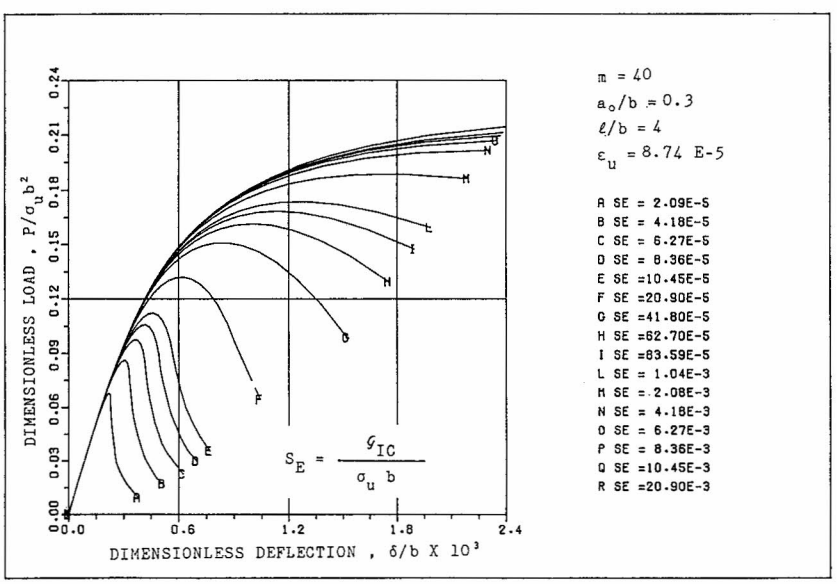

Fig. 10(b).

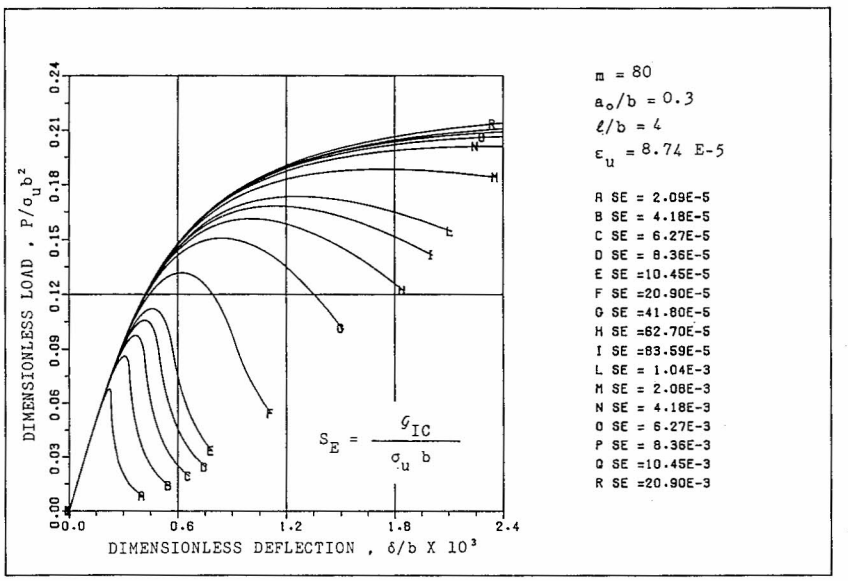

Fig. 10(c).

Fig. 10. Dimensionless load–deflection response of an initially cracked specimen ($a_0/b = 0.3$), by varying the brittleness number, $s_E = G_{IC}/\sigma_u b = w_c/2b$, between 2×10^{-5} and 2×10^{-2}. (a) $m = 20$, (b) $m = 40$, (c) $m = 80$.

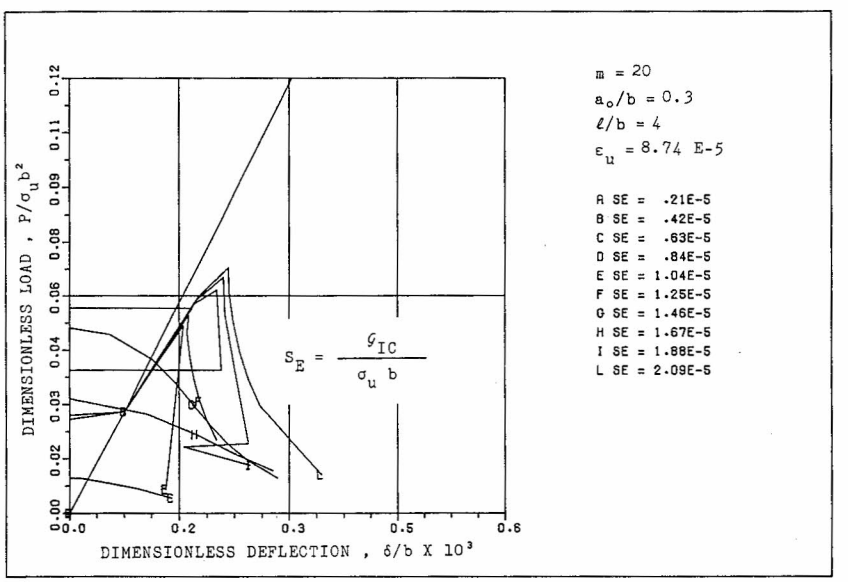

Fig. 11(a).

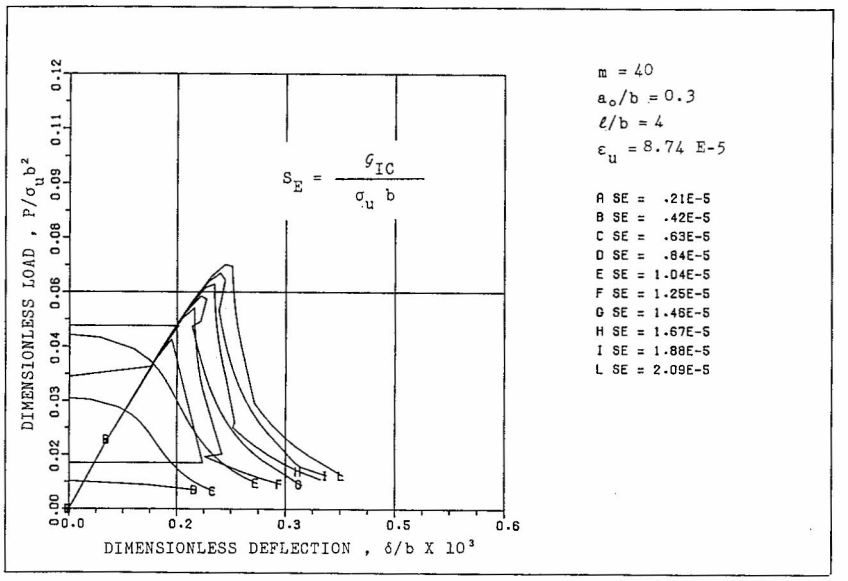

Fig. 11(b).

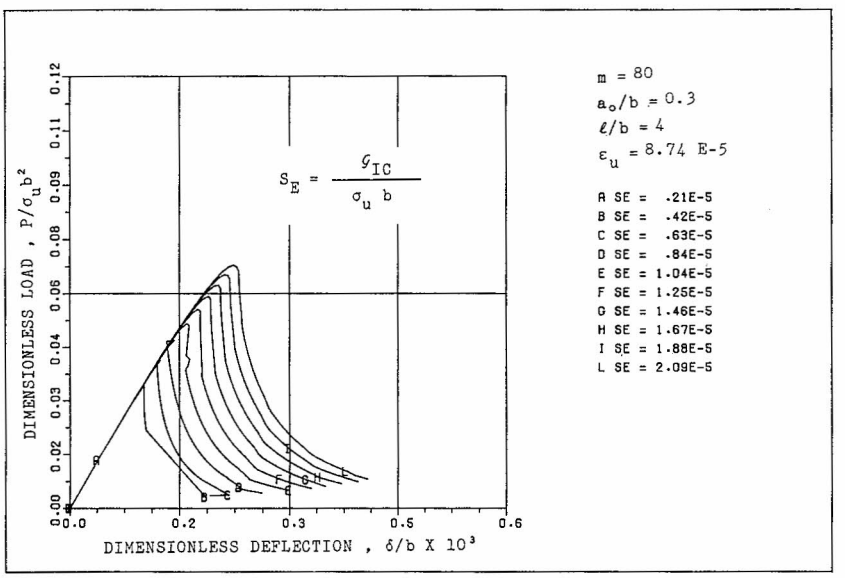

Fig. 11(c).

Fig. 11. Dimensionless load–deflection response of an initially cracked specimen ($a_0/b = 0.3$), by varying the brittleness number, $s_E = G_{IC}/\sigma_u b = w_c/2b$, between 2×10^{-6} and 2×10^{-5}. (a) $m = 20$, (b) $m = 40$, (c) $m = 80$.

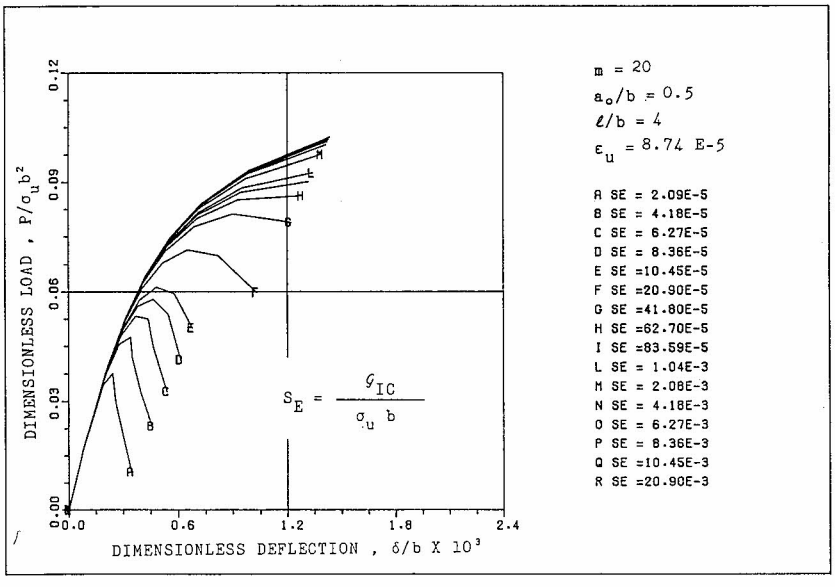

Fig. 12(a).

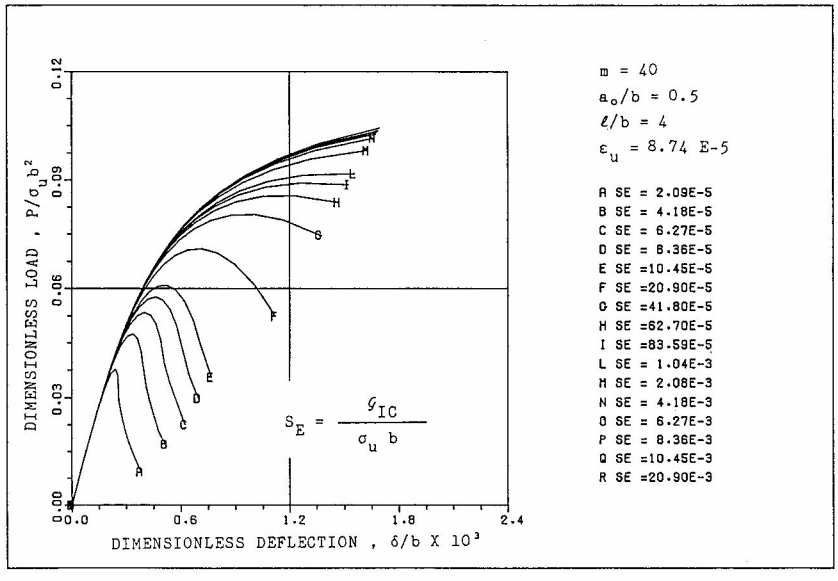

Fig. 12(b).

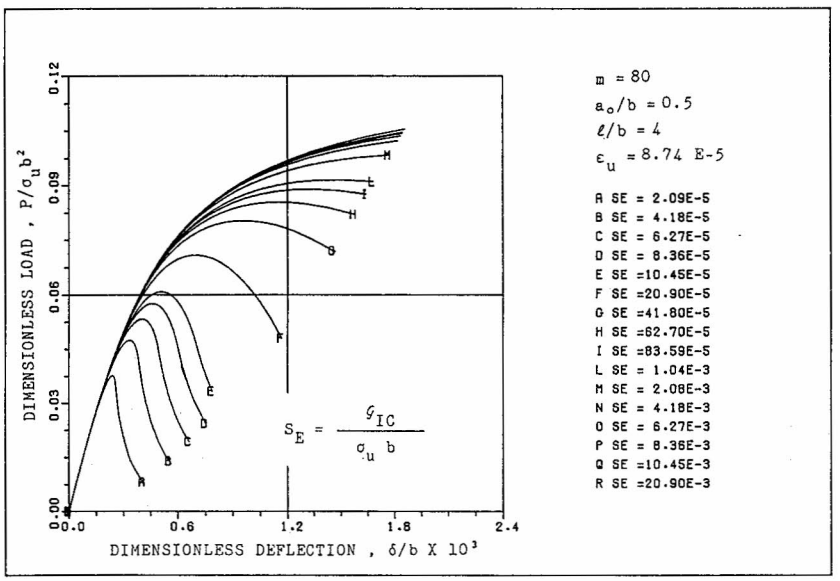

Fig. 12(c).

Fig. 12. Dimensionless load–deflection response of an initially cracked specimen ($a_0/b = 0.5$), by varying the brittleness number, $s_E = G_{IC}/\sigma_u b = w_c/2b$, between 2×10^{-5} and 2×10^{-2}. (a) $m = 20$, (b) $m = 40$, (c) $m = 80$.

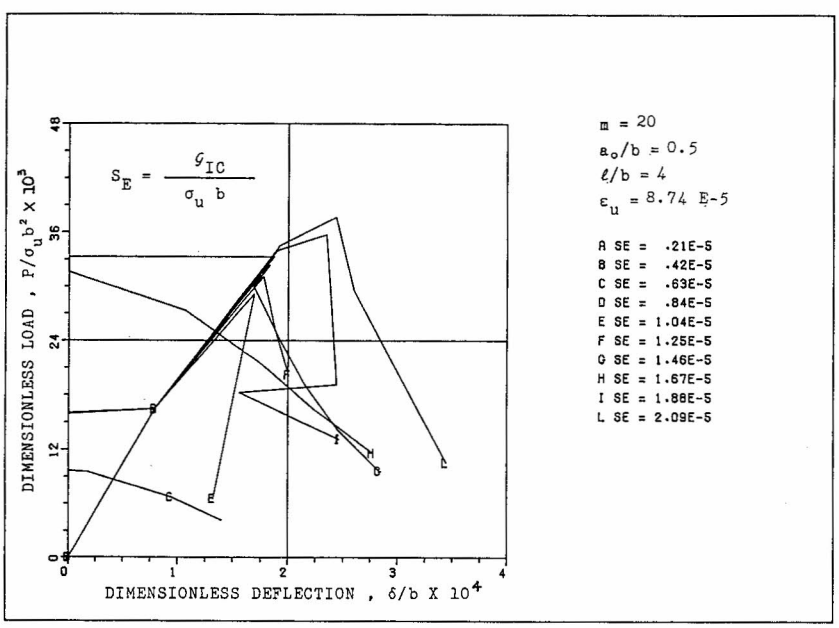

Fig. 13(a).

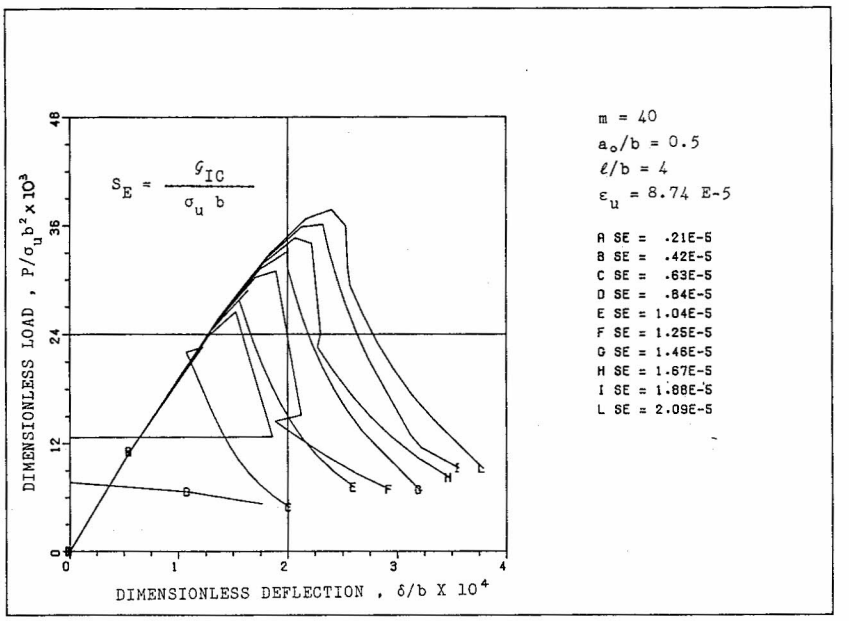

Fig. 13(b).

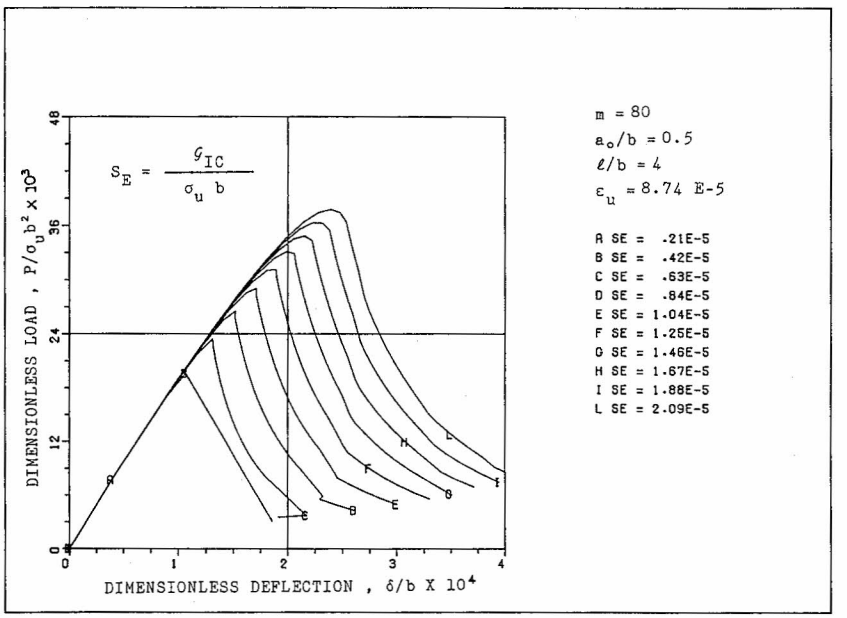

Fig. 13(c).

Fig. 13. Dimensionless load–deflection response of an initially cracked specimen ($a_0/b = 0.5$), by varying the brittleness number $s_E = G_{IC}/\sigma_u b = w_c/2b$, between 2×10^{-6} and 2×10^{-5}. (a) $m = 20$, (b) $m = 40$, (c) $m = 80$.

From the cases shown in Figs 6 and 7, the s_E threshold below which the results are unacceptable is approximately

$$s_E = \frac{w_c}{2mh} \simeq \frac{80}{m} \times 10^{-5}. \tag{8}$$

The lower bound to s_E can be regarded as an upper bound to the finite element size h:

$$h \lesssim 600 w_c. \tag{9}$$

For a normal concrete with maximum aggregrate size of 2 cm, $w_c \simeq 0.1$ mm and then eqn. (9) gives $h \lesssim 6$ cm.

The load–deflection response shows the same trends even when an initial crack is present in the lower edge of the three-point bending beam. The following initial crack depths are considered: $a_0/b = 0.1$ (Figs 8 and 9), $a_0/b = 0.3$ (Figs 10 and 11), $a_0/b = 0.5$ (Figs 12 and 13). The deeper the initial crack is, the more ductile the resulting beam behaviour is, as will be further discussed in the next section.

4. INFLUENCE OF THE INITIAL CRACK DEPTH

A three-point bending test specimen of depth $b = 15$ cm, thickness $t = b = 15$ cm and span $l = 4b = 60$ cm is considered. The finite element mesh in Fig. 5(b) ($m = 40$) is utilized in the numerical simulation of a concrete-like material with the following mechanical properties: Young's modulus $E = 365{,}000$ kg/cm^2, tensile strength $\sigma_u = 31.90$ kg/cm^2, Poisson ratio $\nu = 0.10$. For two different values of fracture toughness, $G_{IC} = 0.05$ and 0.01 kg/cm respectively, the initial crack depth a_0/b is varied from 0.0 (initially uncracked specimen) to 0.5. For all the cases considered, the load–deflection (P–δ) and load–crack mouth opening displacement (P–w_1) curves are obtained.

The P–δ curves in Fig. 14(a) are related to different initial crack depths. Obviously, stiffness and maximum loading capacity of the specimen decrease by increasing the initial crack depth a_0/b. On the other hand, even the slope of the softening branch decreases, so that the uncracked specimen reveals considerable instability and a nearly vertical drop in its loading capacity, whereas the cracked specimens appear much more ductile and controllable in the P–δ descending stage. The terminal softening branch appears as totally independent of the initial crack depth. This is a direct consequence of the assumption of a damage zone collinear to the crack and concentrated on a line of zero thickness.

The P–δ curves in Fig. 14(b) describe the specimen behaviour when $G_{IC} = 0.01$ kg/cm. For $a_0/b \leqslant 0.25$ a snap-back instability occurs [14–18], namely, a softening branch with positive slope ($\mathrm{d}P/\mathrm{d}\delta > 0$) is revealed. If the loading process is controlled by the deflection, the loading capacity will show a discontinuity with a negative jump and the representative point will drop on the fourth branch of the P–δ curve (Fig. 15). The part BD of the P–δ curve in Fig. 15 appears as a virtual path, which can be revealed only by decreasing both load and deflection while the crack grows and opens. The four stages of the P–δ diagram in Fig. 15 can be defined as follows:

$$(OA)\ \dot{P} > 0, \quad \dot{\delta} > 0, \quad \dot{a} \geqslant 0, \quad \dot{w}_1 \geqslant 0; \tag{10a}$$

$$(AB)\ \dot{P} < 0, \quad \dot{\delta} > 0, \quad \dot{a} \geqslant 0, \quad \dot{w}_1 > 0; \tag{10b}$$

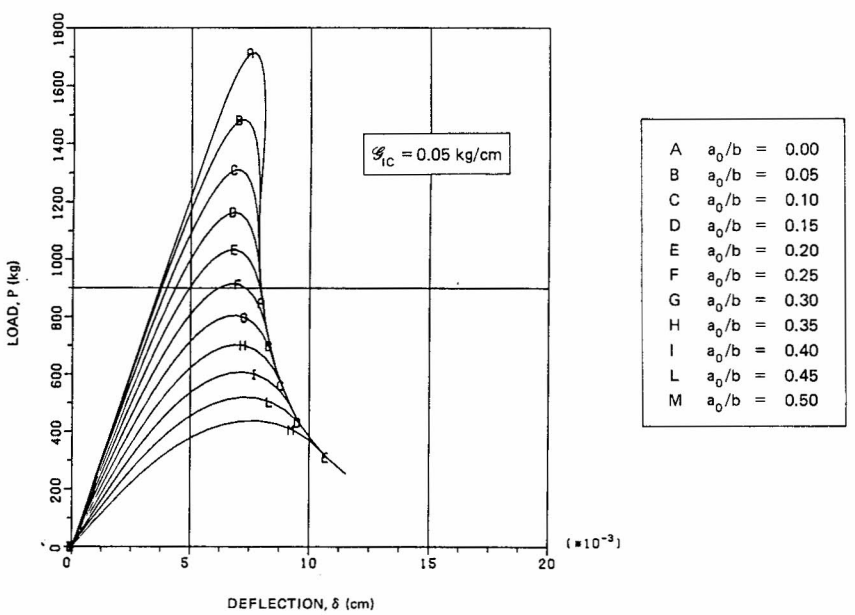

Fig. 14(a).

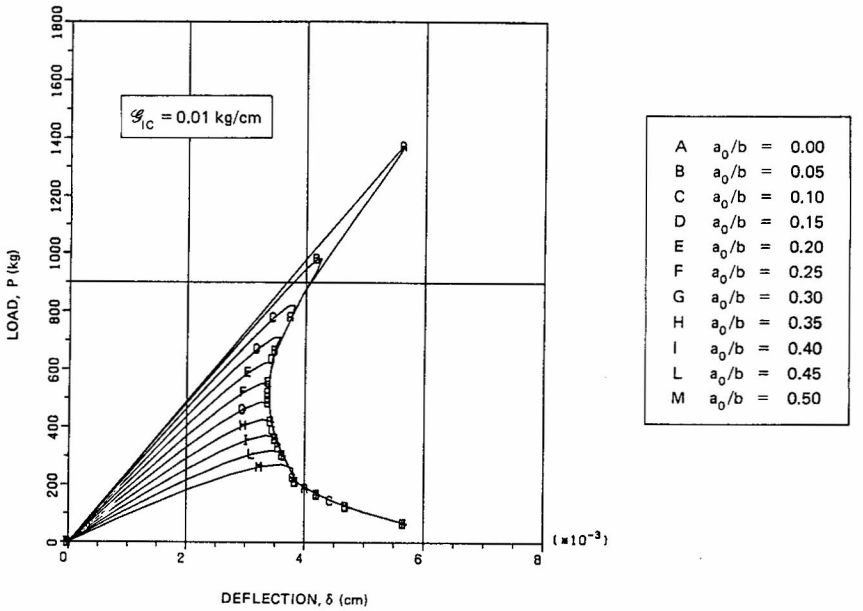

Fig. 14(b).

Fig. 14. Load–deflection plots by varying the initial crack depth a_0/b. (a) $G_{IC} = 0.05$ kg/cm; (b) $G_{IC} = 0.01$ kg/cm.

$$(BC)\ \mathring{P} < 0, \quad \mathring{\delta} < 0, \quad \mathring{a} > 0, \quad \mathring{w}_1 > 0; \tag{10c}$$

$$(CD)\ \mathring{P} < 0, \quad \mathring{\delta} > 0, \quad \mathring{a} > 0, \quad \mathring{w}_1 > 0; \tag{10d}$$

where the dot indicates derivative with respect to a quantity increasing monotonically with time (e.g. time itself or crack length). For the cases investigated numerically, points A and B tend to coincide, so that a sharp bifurcation in the P–δ path is revealed, as shown in Fig 14(b).

The catastrophic drop in the loading capacity may be avoided and the P–δ snap-back behaviour experimentally shown by controlling the crack mouth opening displacement w_1, instead of the beam deflection δ [14]. In fact, as shown in Fig. 16(a,b), w_1 increases monotonically in the softening stage during the crack propagation.

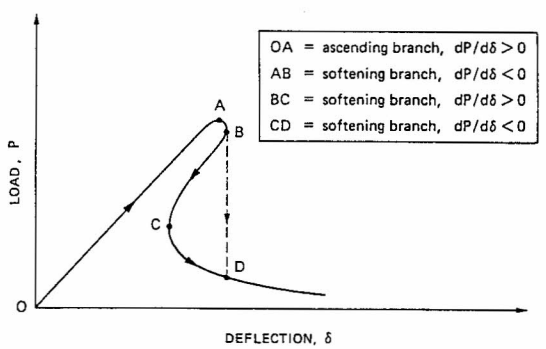

Fig. 15. Catastrophic softening behaviour.

5. INFLUENCE OF SLENDERNESS AND ULTIMATE TENSILE STRAIN

In addition to the slenderness $l/b = 4$ considered in Sec. 3, the ratios $l/b = 8$ and 16 are herein contemplated. For initially uncracked specimens ($a_0/b = 0.0$), Fig. 6(b) ($l/b = 4$) is to be compared with Fig. 17(a) ($l/b = 8$) and Fig. 17(b) ($l/b = 16$). Increase in brittleness with the slab slenderness is manifest also for initially cracked specimens in Fig. 18 ($a_0/b = 0.3$).

Two different ultimate tensile strains are then taken into consideration: $\varepsilon_u = 17.48 \times 10^{-5}$ and 34.96×10^{-5}, in addition to the value $\varepsilon_u = 8.74 \times 10^{-5}$ of Sec. 3. For $a_0/b = 0.0$, the results are reported in Fig. 19, whereas the case $a_0/b = 0.3$ is plotted in Fig. 20. A brittleness increase appears by increasing the ultimate tensile strain.

Both the trends described in this section are due to the variation in the elastic compliance of the non-damaged zone. An increase of such a compliance produces an increase of brittleness in the system. In the softening stage, in fact, the elastic recovery prevails over the localized increase of deformation, so that a snap-back instability occurs.

6. SIZE-SCALE EFFECTS: DECREASE OF APPARENT STRENGTH AND INCREASE OF FICTITIOUS FRACTURE TOUGHNESS

The maximum loading capacity $P^{(1)}_{max}$ of initially uncracked specimens with $l = 4b$ is obtained from

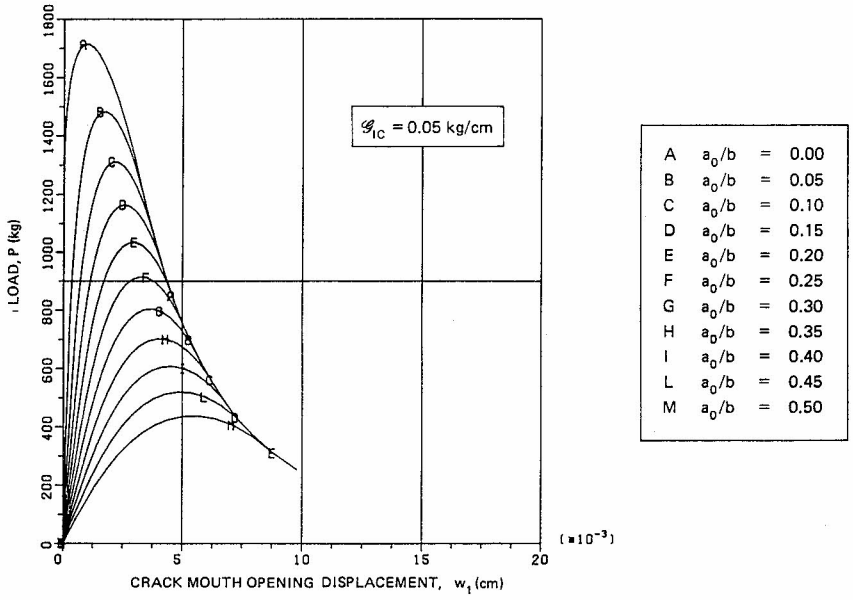

Fig. 16(a).

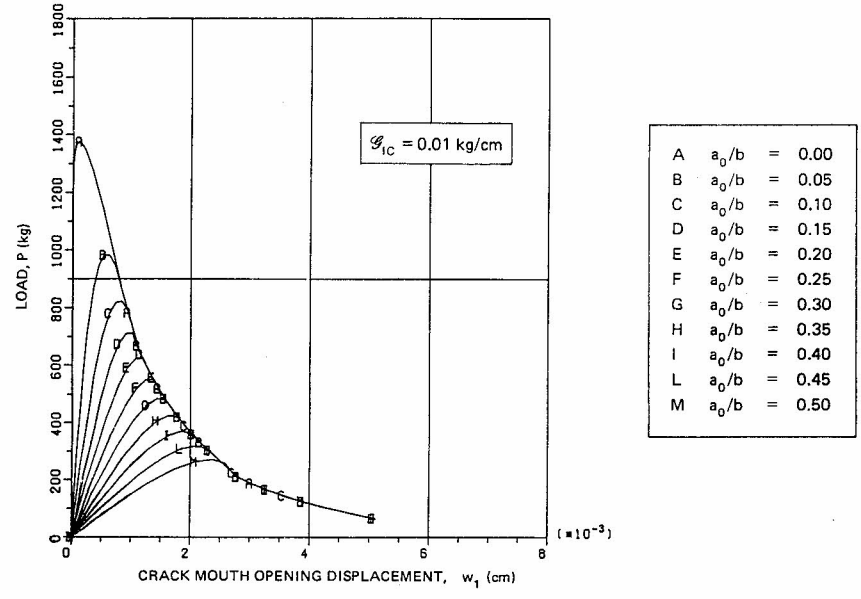

Fig. 16(b).

Fig. 16. Load–crack mouth opening displacement plots by varying the initial crack depth a_0/b. (a) $G_{IC} = 0.05$ kg/cm; (b) $G_{IC} = 0.01$ kg/cm.

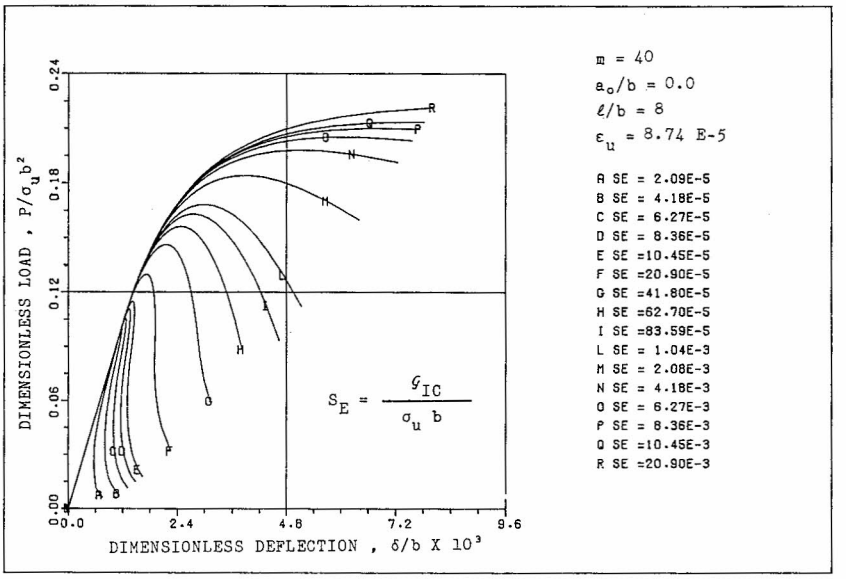

Fig. 17(a).

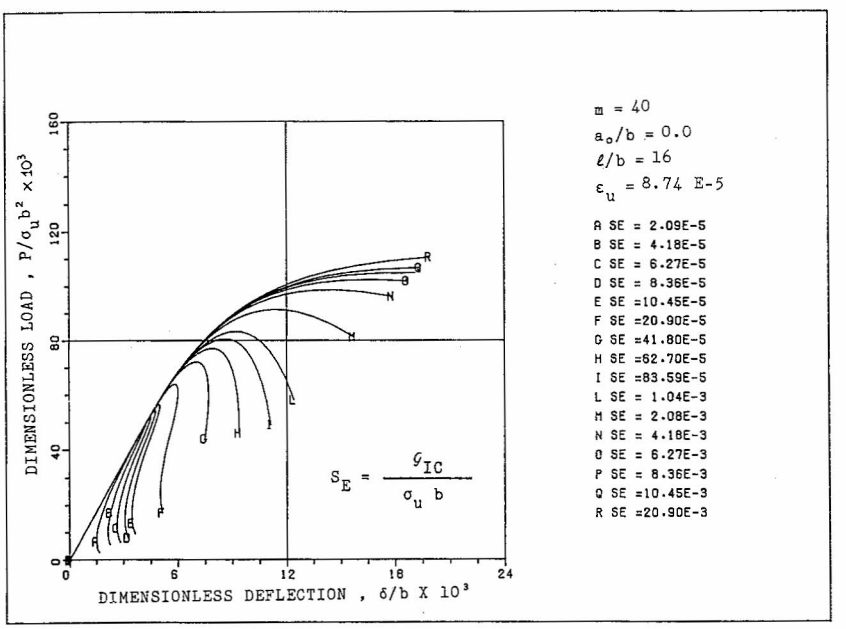

Fig. 17(b).

Fig. 17. Dimensionless load–deflection response of an initially uncracked specimen, by varying the brittleness number, $s_E = G_{IC}/\sigma_u b = w_c/2b$, between 2×10^{-5} and 2×10^{-2}. (a) $l/b = 8$; (b) $l/b = 16$.

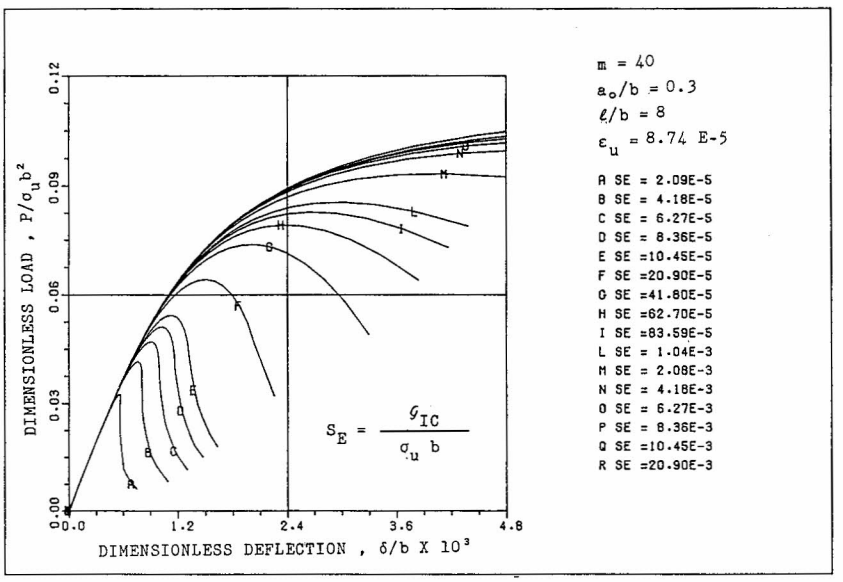

Fig. 18(a).

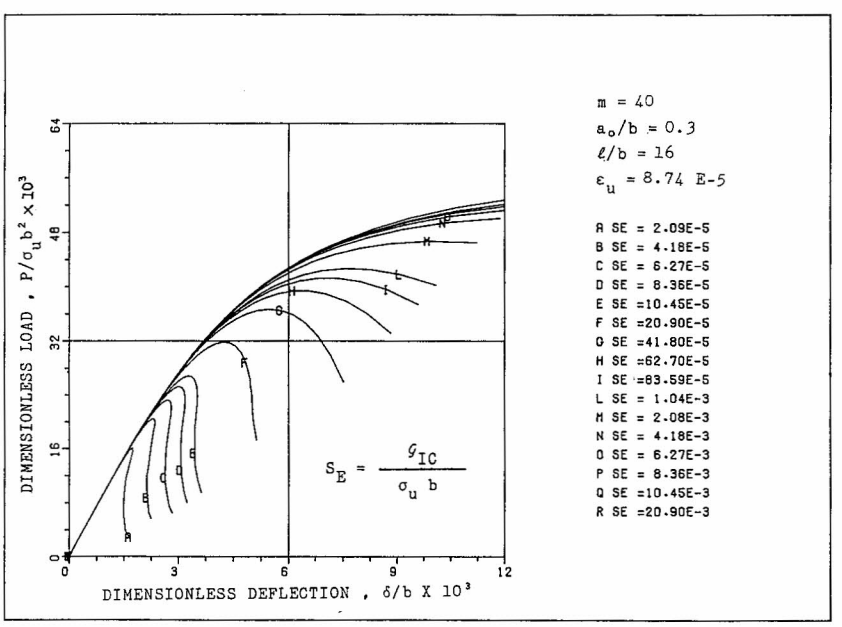

Fig. 18(b).

Fig. 18. Dimensionless load–deflection response of an initially cracked specimen ($a_0/b = 0.3$), by varying the brittleness number, $s_E = G_{IC}/\sigma_u b = w_c/2b$, between 2×10^{-5} and 2×10^{-2}. (a) $l/b = 8$; (b) $l/b = 16$.

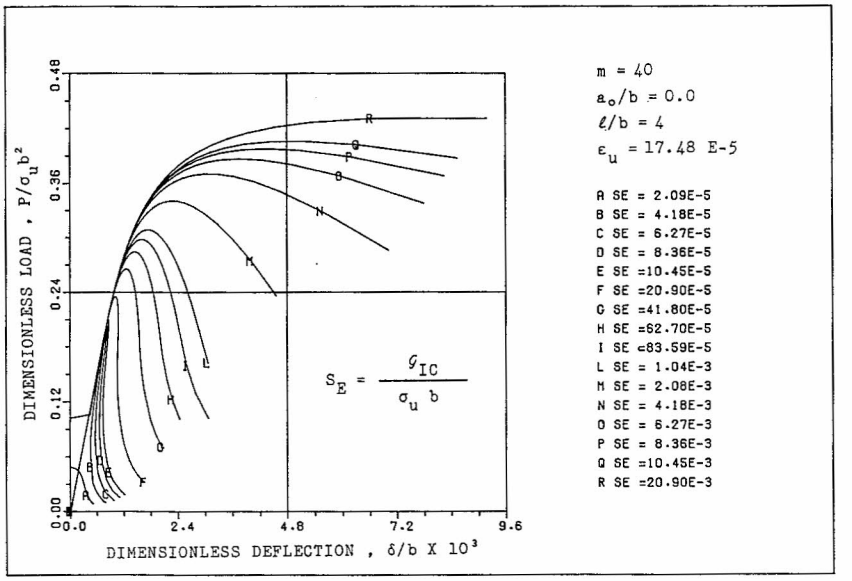

Fig. 19(a).

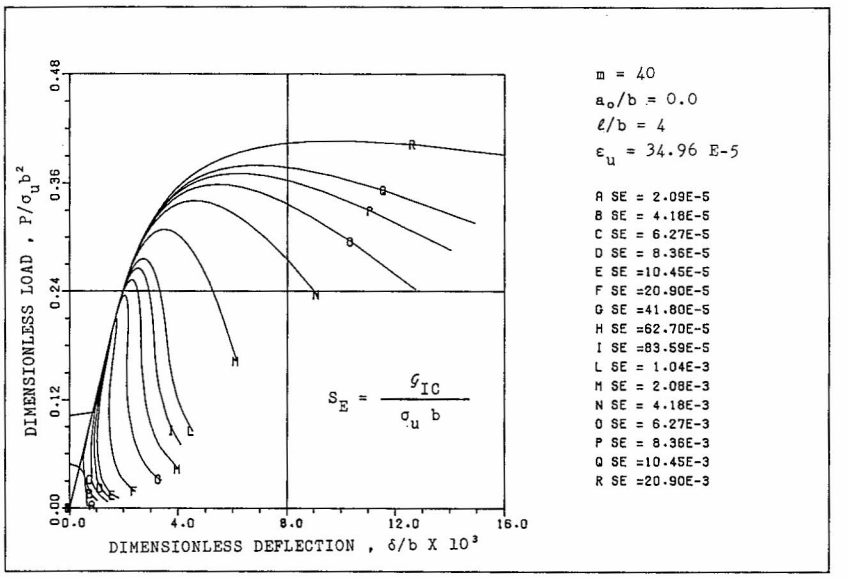

Fig. 19(b).

Fig. 19. Dimensionless load–deflection response of an initially uncracked specimen, by varying the brittleness number, $s_E = G_{IC}/\sigma_u b = w_c/2b$, between 2×10^{-5} and 2×10^{-2}. (a) $\varepsilon_u = 17.48 \times 10^{-5}$; (b) $\varepsilon_u = 34.96 \times 10^{-5}$.

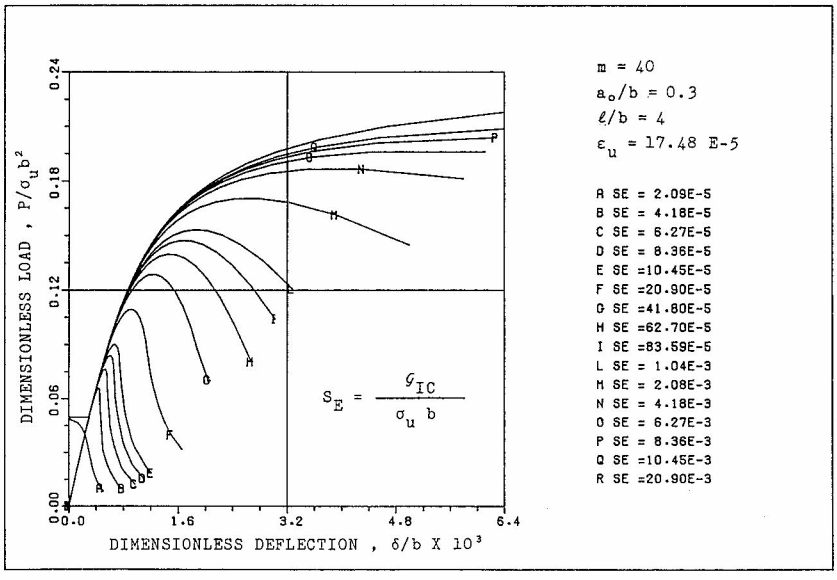

Fig. 20(a).

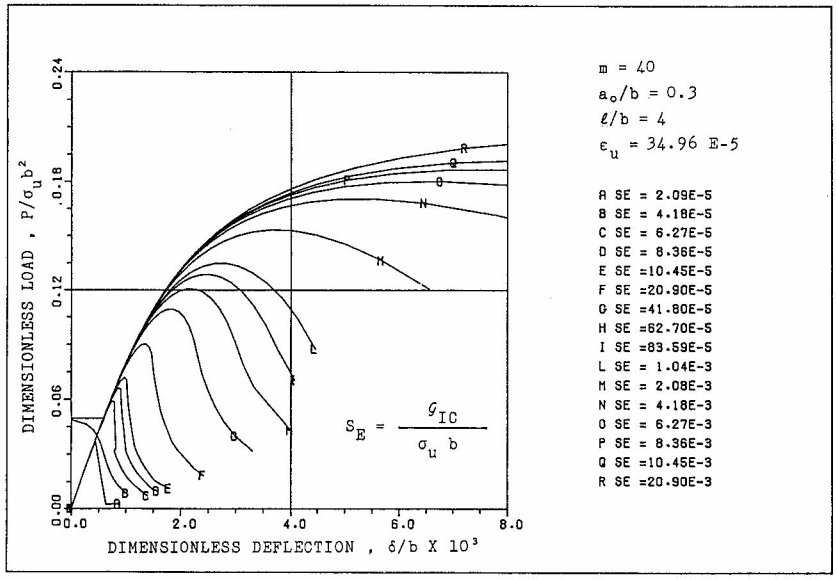

Fig. 20(b).

Fig. 20. Dimensionless load–deflection response of an initially cracked specimen ($a_0/b = 0.3$), by varying the brittleness number, $s_E = G_{IC}/\sigma_u b = w_c/2b$, between 2×10^{-5} and 2×10^{-2}. (a) $\varepsilon_u = 17.48 \times 10^{-5}$; (b) $\varepsilon_u = 34.96 \times 10^{-5}$.

Figs 6 and 7. On the other hand, the maximum load $P^{(3)}_{max}$ of ultimate strength is given by

$$P^{(3)}_{max} = \frac{2}{3}\frac{\sigma_u t b^2}{l}. \quad (11)$$

The values of the ratio $P^{(1)}_{max}/P^{(3)}_{max}$ may also be regarded as the ratio of the apparent tensile strength σ_f [given by the maximum load $P^{(1)}_{max}$ and applying eqn. (11)] to the true tensile strength σ_u (considered as a material constant). It is evident from Fig. 21 that the results of the cohesive crack model tend to those of the ultimate strength analysis for low s_E values:

$$\lim_{s_E \to 0} P^{(1)}_{max} = P^{(3)}_{max}. \quad (12)$$

Therefore, only for comparatively large specimen sizes can the tensile strength σ_u be obtained as $\sigma_u = \sigma_f$. With the usual laboratory specimens, an apparent strength higher than the true one is always found.

The maximum loading capacity $P^{(1)}_{max}$ of initially cracked specimens according to the cohesive crack model is obtained from the P–δ diagrams in Figs 8–13. On the other hand, the maximum loading capacity $P^{(2)}_{max}$ according to LEFM can be derived from the following formula [19]:

$$P^{(2)}_{max} = \frac{K_{IC} t b^{3/2}}{l\, g(a_0/b)} \quad (13)$$

with the shape-function g given by

$$g\left(\frac{a_0}{b}\right) = 2.9\left(\frac{a_0}{b}\right)^{1/2} - 4.6\left(\frac{a_0}{b}\right)^{3/2} + 21.8\left(\frac{a_0}{b}\right)^{5/2} - 37.6\left(\frac{a_0}{b}\right)^{7/2} + 38.7\left(\frac{a_0}{b}\right)^{9/2},$$

and the critical value of stress-intensity factor K_{IC} computed according to the well-known relationship

$$K_{IC} = \sqrt{G_{IC} E}. \quad (14)$$

Eventually, a simple ultimate strength analysis on the center-line with the assumption of a butterfly stress variation through the ligament, gives

$$P^{(3)}_{max} = \frac{2}{3}\frac{\sigma_u t (b - a_0)^2}{l}. \quad (15)$$

The values of the ratios $P^{(1)}_{max}/P^{(2)}_{max}$ and $P^{(3)}_{max}/P^{(2)}_{max}$ are reported as functions of the inverse of the brittleness number s_E in Fig. 22. The values $\varepsilon_u = 8.7 \times 10^{-5}$, $t = b$, $l = 4b$ are assumed. The ratio $P^{(1)}_{max}/P^{(2)}_{max}$ may also be regarded as the ratio of the fictitious fracture toughness (given by the nonlinear maximum load) to the true fracture toughness (considered as a material constant).

It is evident that, for high s_E numbers, the ultimate strength collapse results in a more critical condition than that of LEFM ($P^{(3)}_{max} < P^{(2)}_{max}$); also, the results of the cohesive crack model tend to those of LEFM for low s_E values:

$$\lim_{s_E \to 0} P^{(1)}_{max} = P^{(2)}_{max}. \quad (16)$$

The fictitious crack depth at the maximum load is reported as a function of the inverse of the brittleness number s_E in Fig. 23. The increase in the structure brittleness for $s_E \to 0$ is evident also from this diagram, the process zone at $dP/d\delta = 0$ tending to disappear, whereas it tends to cover the whole ligament for $s_E \to \infty$ (ductile collapse). The real (or stress-free) crack depth at the maximum load is nearly coincident with the initial crack depth for each value of s_E. This means that the slow crack growth does not start before the softening stage.

7. INFLUENCE OF THE SHAPE OF THE COHESIVE DIAGRAM σ–w

Let us consider a three-point bending test specimen with geometrical ratios $l = 4b$ and $t = b$ (Fig. 3) and a central crack of depth $a_0/b = 0.1$, and a material with ultimate strain $\varepsilon_u = 8.7 \times 10^{-5}$ and Poisson ratio $\nu = 0.1$. A bilinear σ–w diagram is assumed (Fig. 1c) with the knee at the point of coordinates $w = 2/9\, w_{eq}$, $\sigma = 1/3\sigma_u$. The dimensionless load–deflection diagrams are represented in Fig. 24 by varying the brittleness number s_E.

The ratio of the maximum loading capacity obtained by the cohesive crack model to the maximum loading according to LEFM is equal to the ratio of the fictitious fracture toughness to the true one, K_{IC}. Such a ratio is demonstrated to tend to unity when $s_E \to 0$, for the linear as well as for the bilinear σ–w constitutive softening relations (Fig. 25). This means that, for large structure sizes and/or low fracture energies, the bifurcation of the load–deflection curve tends to describe the classical LEFM-instability.

Therefore, it is possible to conclude that, although the σ–w shape affects the theoretical value of the maximum load, such a dependence is reduced by decreasing the number s_E. As a limit case, for $s_E \to 0$, the maximum load derives from the well-known LEFM relation: $K_I = K_{IC} = \sqrt{(G_{IC} E)}$, and is dependent only on the area G_{IC} under the assumed σ–w diagram, and not on the shape of this diagram [13, 20].

Acknowledgements—The numerical results reported in the present paper were obtained in a joint research program between ENEL-CRIS-Milano and the University of Bologna.

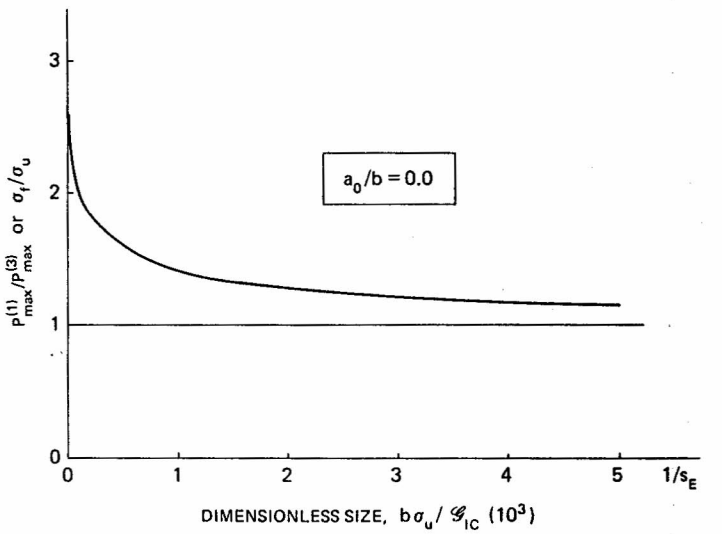

Fig. 21. Decrease of the apparent ultimate tensile strength σ_f, by increasing the specimen size.

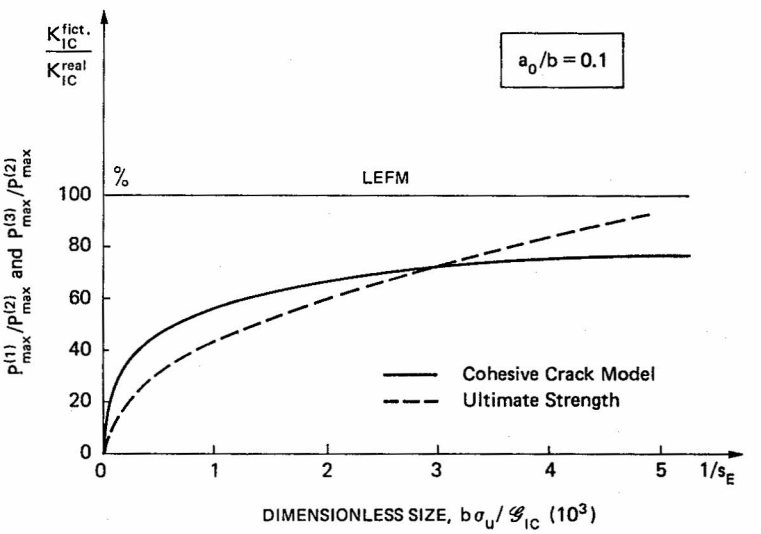

Fig. 22(a).

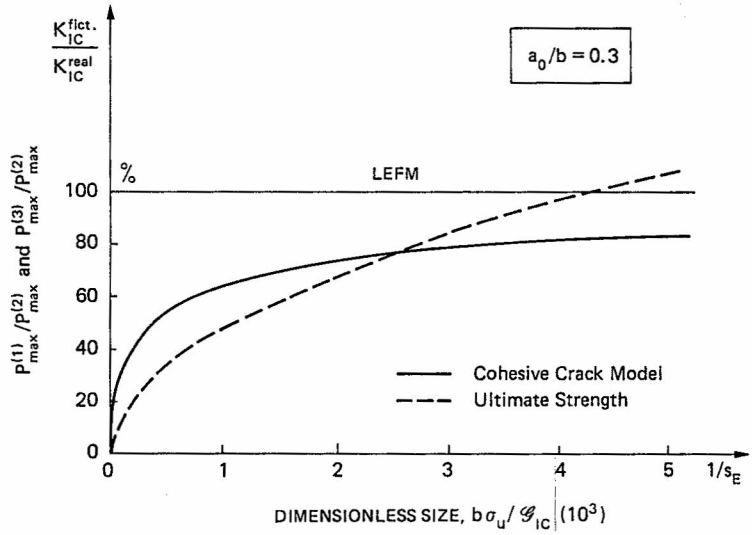

Fig. 22(b).

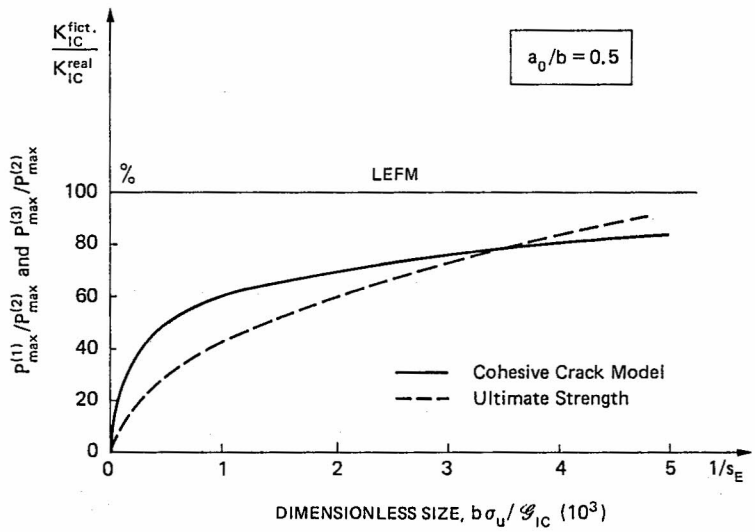

Fig. 22(c).

Fig. 22. Increase of the fictitious fracture toughness $K_{IC}^{fict.}$, by increasing the specimen size. (a) $a_0/b = 0.1$; (b) $a_0/b = 0.3$; (c) $a_0/b = 0.5$.

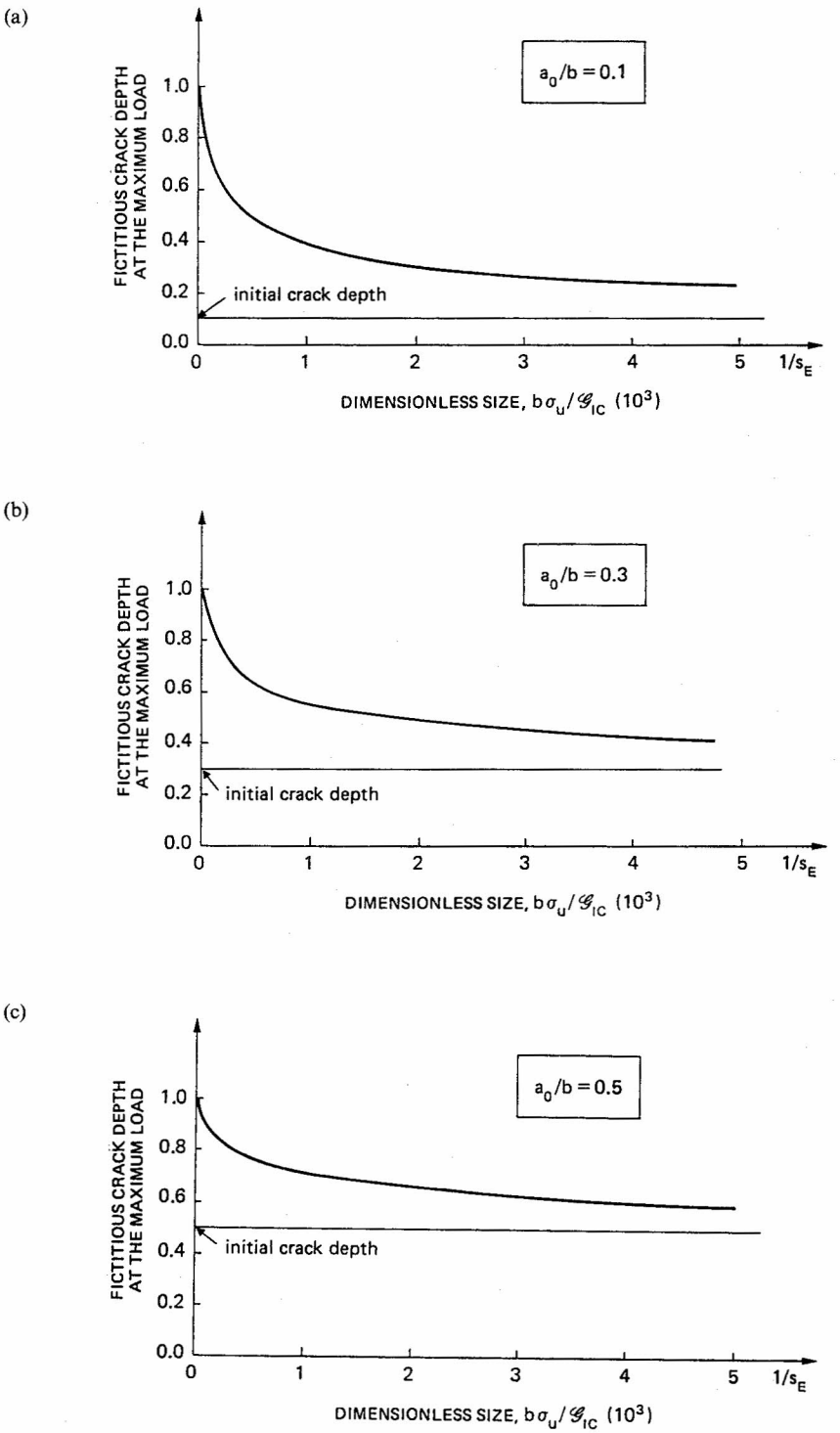

Fig. 23. Fictitious crack depth at the maximum load vs specimen size. (a) $a_0/b = 0.1$; (b) $a_0/b = 0.3$; (c) $a_0/b = 0.5$.

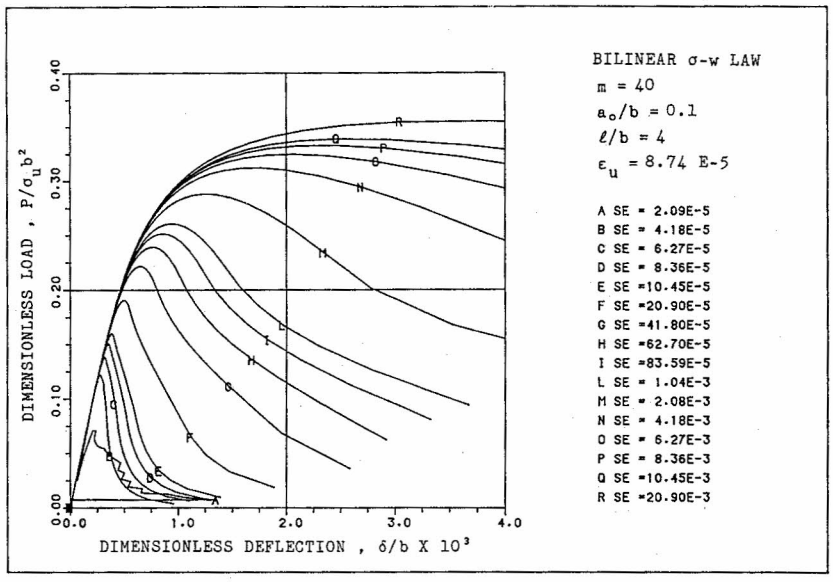

Fig. 24. Dimensionless load–deflection response of an initially cracked specimen ($a_0/b = 0.1$) by varying the brittleness number, $s_E = G_{IC}/\sigma_u b = w_c/2b$, between 2×10^{-5} and 2×10^{-2}, when the bilinear stress–crack opening displacement law in Fig. 1(c) is utilized.

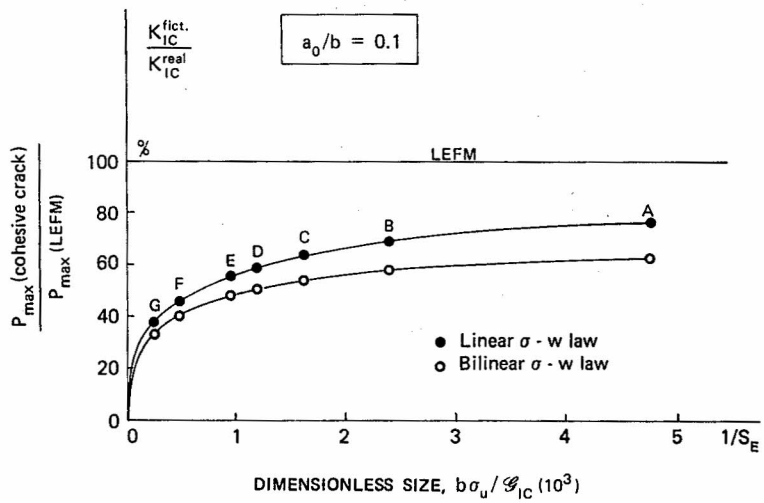

Fig. 25. Size-scale transition toward LEFM instability: linear vs bilinear cohesive law.

REFERENCES

1. A. Carpinteri, Size effect in fracture toughness testing: a dimensional analysis approach. In *Proc. Int. Conf. Analytical and Experimental Fracture Mechanics*, June 23–27, 1980, Rome (Edited by G. C. Sih and M. Mirabile), pp. 785–797. Sijthoff & Noordhoff (1981).
2. A. Carpinteri, Notch sensitivity in fracture testing of aggregative materials. *Engng Fract. Mech.* **16,** 467–481 (1982).
3. A. Carpinteri, C. Marega and A. Savadori, Ductile–brittle transition by varying structural size. *Engng. Fract. Mech.* **21,** 263–271 (1985).
4. A. Carpinteri and G. C. Sih, Damage accumulation and crack growth in bilinear materials with softening. *Theor. appl. Fract. Mach.* **1,** 145–159 (1984).
5. A. Hillerborg, M. Modeer and P. E. Petersson, Analysis of crack formation and crack growth in concrete by means of fracture mechanics and finite elements. *Cement Concrete Res.* **6,** 773–782 (1976).
6. P. E. Petersson, Crack growth and development of fracture zones in plain concrete and similar materials. Rep. TVBM-1006, Division of Building Materials, Lund Institute of Technology (1981).
7. G. Colombo and E. Limido, A numerical method for the analysis of stable TPBT tests: comparison with some experimental data (in Italian) XI *Convegno Nazionale dell'Associazione Italiana per l'Analisi delle Sollecitazioni*, Torino, pp. 233–243 (1983).
8. A. Carpinteri, Interpretation of the Griffith instability as a bifurcation of the global equilibrium. In *NATO Advanced Research Workshop on Application of Fracture Mechanics to Cementitious Composites*, Evanston, IL, 4–7 September 1984 (Edited by S.P. Shah), pp. 287–316. Martinus Nijhoff (1985).
9. A. Carpinteri, A. Di Tommaso and M. Fanelli, Influence of material parameters and geometry on cohesive crack propagation. In *Proc. Int. Conf. Fracture Mechanics of Concrete*, Lausanne, 1–3 October 1985 (Edited by F. H. Wittmann), *Fracture Toughness and Fracture Energy of Concrete*, pp. 117–135. Elsevier, Amsterdam (1986).
10. A. Carpinteri, G. Colombo and G. Giuseppetti, Accuracy of the numerical description of cohesive crack propagation. In *Proc. Int. Conf. Fracture Mechanics of Concrete*, Lausanne, 1–3 October 1985 (Edited by F. H. Wittmann), *Fracture Toughness and Fracture Energy of Concrete*, pp. 189–195. Elsevier, Amsterdam (1986).
11. A. Carpinteri, Softening instability and equilibrium branching in cohesive solids. In *Euromech Colloquium 198, Physical–Numerical Modelling in Non-linear Fracture Mechanics*, Stuttgart, 11–12 September 1985 (Edited by J. H. Argyris) (in press).
12. A. Carpinteri and M. Fanelli, Numerical analysis of the catastrophic softening behaviour in brittle structures. In *Proc. 4th Int. Conf. Numerical Methods in Fracture Mechanics*, San Antonio, TX, 23–27 March 1987, pp. 369–386. Pineridge Press, Swansea (1987).
13. A. Carpinteri, G. Colombo, G. Ferrara and G. Giuseppetti, Numerical simulation of concrete fracture through a bilinear softening stress–crack opening displacement law. In *Proc. SEM-RILEM Int. Conf. Fracture of Concrete and Rock*, Houston, TX, 17–19 July 1987 (Edited by S. P. Shah and S. E. Swartz), pp. 178–191.
14. L. Biolzi, S. Cangiano, G. P. Tognon and A. Carpinteri, Snap-back softening instability in high strength concrete beams. In *Proc. SEM-RILEM Int. Conf. Fracture of Concrete and Rock*, Houston, TX, 17–19 June 1987 (Edited by S. P. Shah and S. E. Swartz) (in press).
15. G. Maier, On the unstable behaviour in elastic–plastic beams in flexure (in Italian). *Ist. Lombardo, Accad. Sci. Lett. Rc. Classe Sci.* (A), **102,** 648–677 (1968).
16. C. Fairhurst, J. A. Hudson and E. T. Brown, Optimizing the control of rock failure in servo-controlled laboratory tests. *Rock Mech.* **3,** 217–224 (1971).
17. K. Rokugo, S. Ohno and W. Koyanagi, Automatical measuring system of load–displacement curves including post-failure region of concrete specimens. In *Proc. Int. Conf. Fracture Mechanics of Concrete*, Lausanne, 1–3 October 1985 (Edited by F. H. Wittmann), *Fracture Toughness and Fracture Energy of Concrete*, pp. 403–411. Elsevier, Amsterdam (1986).
18. J. G. Rots, D. A. Hodijk and R. de Borst, Numerical simulation of concrete fracture in direct tension. In *Proc. 4th Int. Conf. Numerical Methods in Fracture Mechanics*, San Antonio, TX, 23–27 March 1987, pp. 457–471. Pineridge Press, Swansea (1987).
19. Standard method of test for plane strain fracture toughness of metallic materials, E 399-74, ASTM.
20. P. E. Roelfstra and F. H. Wittmann, Numerical method to link strain softening with failure of concrete. In *Proc. Int. Conf. Fracture Mechanics of Concrete*, Lausanne, 1–3 October 1985 (Edited by F. H. Wittmann), *Fracture Toughness and Fracture Energy of Concrete*, pp. 163–175. Elsevier, Amsterdam (1986).